2

Crop Disease and Pest Monitoring by Remote Sensing

Wenjiang Huang, Juhua Luo, Jingcheng Zhang,
Jinling Zhao, Chunjiang Zhao, Jihua Wang,
Guijun Yang, Muyi Huang, Linsheng Huang and Shizhou Du
Beijing Research Center for Information Technology in Agriculture, Beijing China

1. Introduction

Plant diseases and pests can affect a wide range of commercial crops, and result in a significant yield loss. It is reported that at least 10% of global food production is lost due to plant diseases (Christou and Twyman, 2004; Strange and Scott, 2005). Excessive pesticides are used for protecting crops from diseases and pests. This not only increases the cost of production, but also raises the danger of toxic residue in agricultural products. Disease and pest control could be more efficient if disease and pest patches within fields can be identified timely and treated locally. This requires obtaining the information of disease infected boundaries in the field as early and accurately as possible. The most common and conventional method is manual field survey. The traditional ground-based survey method requires high labor cost and produces low efficiency. Thus, it is unfeasible for large area. Fortunately, remote sensing technology can provide spatial distribution information of diseases and pests over a large area with relatively low cost. The presence of diseases or insect feedings on plants or canopy surface causes changes in pigment, chemical concentrations, cell structure, nutrient, water uptake, and gas exchange. These changes result in differences in color and temperature of the canopy, and affect canopy reflectance characteristics, which can be detectable by remote sensing (Raikes and Burpee 1998). Therefore, remote sensing provides a harmless, rapid, and cost-effective means of identifying and quantifying crop stress from differences in the spectral characteristics of canopy surfaces affected by biotic and abiotic stress agents.

This chapter introduces some successful studies about detecting and discriminating yellow rust and aphid (economically important disease and pest in winter wheat in China) using field, airborne and satellite remote sensing.

2. Detecting yellow rust of winter wheat by remote sensing

Yellow rust *(Biotroph Puccinia striiformis),* also known as stripe rust, is a fungal disease of winter wheat *(Triticum aestivum L.).* It produces leaf lesions (pustules), which are yellow in color and tend to be grouped in patches. Yellow rust often occurs in narrow stripes, 2–3 mm wide that run parallel to the leaf veins. Yellow rust is responsible for approximately 73–85%

of recorded yield losses, and grain quality is also significantly reduced (Li et al. 1989). Consequently, effective monitoring of the incidence and severity of yellow rust in susceptible regions is of great importance to guide the spray of pesticides and to provide data for the local agricultural insurance services. Fortunately, remote sensing technology provides a possible way to detect the incidence and severity of the disease rapidly.

The interaction of electromagnetic radiation with plants varies with the wavelength of the radiation. The same plant leaves may exhibit significant different reflectance depending on the level of health and or vigor (Wooley 1971, West et al. 2003, Luo et al., 2010). Healthy and vigorously growing plant leaves will generally have

1. Low reflectance at visible wavelengths owing to strong absorption by photoactive pigments (chlorophylls, anthocyanins, carotenoids).
2. High reflectance in the near infrared because of multiple scattering at the air-cell interfaces in the leaf's internal tissue.
3. Low reflectance in wide wavebands in the short-wave infrared because of absorption by water, proteins, and other carbon constituents.

The incidence and severity of yellow rust can be monitored according to the differences of spectral characteristics between healthy and disease plants. In this chapter, we will report several successful studies on the detection and identification of yellow rust in winter wheat by remote sensing.

2.1 Detecting and discriminating yellow rust at canopy level

Hyperspectral remote sensing is one of the advanced and effective techniques in disease monitoring and mapping. However, the difficulty in discriminating a disease from common nutrient stresses largely hampers the practical use of this technique. This is because some common nutrient stresses such as the shortage or overuse of nitrogen or water could have similar variations of biochemical properties and plant morphology, and therefore result in similar spectral responses. However, for the remedial procedures for stressed crops, there is a significant difference between disease and nutrient stresses. For example, applying fungicide to water-stressed crops would lead to a disastrous outcome. Therefore, to discriminate yellow rust from common nutrient stresses is of practical importance to crop growers or landowners.

The specific objectives of this study are to: (1) systematically test the sensitivity and consistency of several commonly used spectral features to yellow rust disease during major growth stages; (2) for those spectral features that are consistently sensitive to yellow rust disease, we will further examine their sensitivity to nutrient stresses to determine whether there are specifically sensitive to yellow rust disease, but insensitive to water and nitrogen stresses.

2.1.1 Materials and methods

2.1.1.1 Experimental design and field conditions

The experiments were conducted at Beijing Xiaotangshan Precision Agriculture Experimental Base, in Changping district, Beijing (40°10.6'N, 116°26.3'E) for the growing seasons of 2001-2002 and 2002-2003. Table 1 summarizes the soil properties including

organic matter, total nitrogen, alkali-hydrolysis nitrogen, available phosphorus and available potassium for both growing seasons. Three cultivars of winter wheat used in 2001-2002 experiment (2002 Exp) were Jingdong8, Jing9428 and Zhongyou9507, while the cultivars used in 2002-2003 (2003 Exp) were Xuezao, 98-100 and Jing411. All the cultivars applied in both growing seasons included erective, middle and loose with respect to the canopy morphology.

Items		Disease inoculation experiment	Nutrient stress experiment
Growth period		Sep 2002-Jun 2003	Sep 2001-Jun 2002
Top soil nutrient status (0-0.3m depth)	Organic matter	1.42%-1.48%	1.21%-1.32%
	Total nitrogen	0.08%-0.10%	0.092%-0.124%
	Alkali-hydrolysis nitrogen	58.6-68.0 mg kg^{-1}	68.8-74.0 mg kg^{-1}
	Available phosphorus	20.1-55.4 mg kg^{-1}	25.2-48.3 mg kg^{-1}
	Rapidly available potassium	117.6-129.1 mg kg^{-1}	96.6-128.8 mg kg^{-1}
Cultivars		Xuezao, 98-100, Jing411	Jingdong8, Jing9428, Zhongyou9507
Treatments		Normal; YR1: 3mg 100^{-1} ml spores solution; YR2: 9mg 100^{-1} ml spores solution; YR3: 12mg 100^{-1} ml spores solution (all treatments applied 200 kg ha^{-1} nitrogen and 450 m^3 ha^{-1} water)	Normal: 200 kg ha^{-1} nitrogen, 450 m^3 ha^{-1} water; W-SD: 200 kg ha^{-1} nitrogen, 225 m^3 ha^{-1} water; W-SED: 200 kg ha^{-1} nitrogen, 0 m^3 ha^{-1} water; N-E: 350 kg ha^{-1} nitrogen, 450 m^3 ha^{-1} water; N-D: 0 kg ha^{-1} nitrogen, 450 m^3 ha^{-1} water; W-SED+N-E: 350 kg ha^{-1} nitrogen, 0 m^3 ha^{-1} water; W-SED+N-D: 0 kg ha^{-1} nitrogen, 0 m^3 ha^{-1} water;
Spectral reflectance measurements (on day after sowing)		207, 216, 225, 230, 233	196, 214, 225, 232, 239

Table 1. Basic information of disease inoculation experiment and nutrient stress experiment

For 2002 Exp, six stress treatments of water and nitrogen were applied, and the treatments were based on local conditions, which usually suffered from yellow rust in the northern part

of China. Each treatment was applied on 0.3 ha area, and the treatments were 200 kg ha^{-1} nitrogen and 225 m^3 ha^{-1} water (slightly deficient water, W-SD),200 kg ha^{-1} nitrogen and no irrigation (seriously deficient water, W-SED), 350 kg ha^{-1} nitrogen and 450 m^3 ha^{-1} water (excessive nitrogen, N-E), no fertilization and 450 m3 ha-1 water (deficient nitrogen, N-D), 350 kg ha^{-1} nitrogen and no irrigation (seriously deficient water and excessive nitrogen, W-SED+N-E), and no fertilization and no irrigation (seriously deficient water and deficient nitrogen, W-SED+N-D). A 0.3 ha reference area (Normal) was applied with the recommended rate which received 200 kg ha^{-1} nitrogen and 450 m^3 ha^{-1} water. Three cultivars were evenly distributed in each treatment plot.

For 2003 Exp, according to the National Plant Protection Standard (Li et al. 1989), three levels of concentration of summer spores of yellow rust were applied, and they were 3 mg 100^{-1} ml^{-1} (Yellow rust 1, YR1), 9 mg 100^{-1} ml^{-1} (Yellow rust 2, YR2) and 12 mg 100^{-1} ml^{-1} (Yellow rust 3, YR3), with a dosage of 5 ml spores solution per square meter. The reference area (Normal) that was not inoculated yet was applied with the recommended amount of fungicide to prevent the occasional infection. Each treatment involved 1.2 ha area, with even constitution of three cultivars. All plots in 2003 Exp received the recommended rates of nitrogen (200 kg ha^{-1}) and water (450 m^3 ha^{-1}).

2.1.1.2 Canopy spectral measurements

A high spectral resolution spectrometer, ASD FieldSpec Pro spectrometer (Analytical Spectral Devices, Boulder, CO, USA) fitted with a 25 field of view fore-optic, was used for in-situ measurement of canopy spectral reflectance for both 2002 Exp and 2003 Exp. All canopy spectral measurements were taken from a height of 1.3m above ground (the height of the wheat is 90±3 cm at maturity). Spectra were acquired in the 350-2,500 nm spectral range at a spectral resolution of 3 nm between 350 nm and 1,050 nm, and 10 nm between 1,050 nm and 2,500 nm. A 40 cm × 40 cm BaSO4 calibration panel was used for calculation of reflectance. All irradiance measurements were recorded as an average of 20 scans at an optimized integration time. Prior to subsequent preprocessing, all spectral curves were resampled with 1 nm interval. All measurements were made under clear blue sky conditions between 10:00 and 14:00 (Beijing Local Time).

The spectral measurements were taken 5 times from 196 days after sowing (DAS) to 239 DAS for 2002 Exp, which covered the growth stages of stem elongation, booting, anthesis and milk development. For 2003 Exp, the spectral measurements were taken 5 times from 207 DAS to 233 DAS, which covered the growth stages of booting, anthesis and milk development. The detailed measurement dates for both experiments were given in Table 1. The stem elongation and anthesis stages are essential for the control of yellow rust development, whereas the milk development stage is important for yield loss assessment.

2.1.1.3 Selection of spectral features

The spectral features that we adopted were related to several commonly used vegetation indices (VIs), which were proved to be sensitive to variations of pigments and stresses. Furthermore, in order to conduct a thorough investigation of various types of spectral features, we also included a number of spectral features that were based on derivative transformation and continuum removal transformation (Gong et al. 2002; Pu et al. 2003;2004). Therefore, the total 38 spectral features are shown in Table 2.

Variable	Definition	Description	Literatures
Derivative transformed spectral variables			
D_b	Maximum value of 1st derivative within blue edge	Blue edge covers 490-530nm. D_b is a maximum value of 1st order derivatives within the blue edge of 35 bands	Gong et al., 2002
λ_b	Wavelength at D_b	λ_b is wavelength position at D_b	Gong et al., 2002
SD_b	Sum of 1st derivative values within blue edge	Defined by sum of 1st order derivative values of 35 bands within the blue edge	Gong et al., 2002
D_y	Maximum value of 1st derivative within yellow edge	Yellow edge covers 550-582nm. D_y is a maximum value of 1st order derivatives within the yellow edge of 28 bands	Gong et al., 2002
λ_y	Wavelength at D_y	λ_y is wavelength position at D_y	Gong et al., 2002
SD_y	Sum of 1st derivative values within yellow edge	Defined by sum of 1st order derivative values of 28 bands within the yellow edge	Gong et al., 2002
D_r	Maximum value of 1st derivative within red edge	Red edge covers 670-737nm. D_r is a maximum value of 1st order derivatives within the red edge of 61 bands	Gong et al., 2002
λ_r	Wavelength at D_r	λr is wavelength position at D_r	Gong et al., 2002
SD_r	Sum of 1st derivative values within red edge	Defined by sum of 1st order derivative values of 61 bands within the red edge	Gong et al., 2002
Continuous removal transformed spectral features			
DEP550-750	The depth of the feature minimum relative to the hull	In the range of 550nm-750nm	Pu et al., 2003;2004
DEP920-1120		In the range of 920nm-1120nm	
DEP1070-1320		In the range of 1070nm-1320nm	
WID550-750	The full wavelength width at half DEP (nm)	In the range of 550nm-750nm	Pu et al., 2003;2004
WID920-1120		In the range of 920nm-1120nm	
WID1070-1320		In the range of 1070nm-1320nm	
AREA550-750	The area of the absorption feature that is the product of DEP and WID	In the range of 550nm-750nm	Pu et al., 2003;2004
AREA920-1120		In the range of 920nm-1120nm	
AREA1070-1320		In the range of 1070nm-1320nm	

Variable	Definition	Description	Literatures
VI-based variables			
GI	Greenness Index	R_{554}/R_{677}	Zarco-Tejada et al., 2005
MSR	Modified Simple Ratio	$(R_{800}/R_{670}-1)/(R_{800}/R_{670}+1)^{1/2}$	Chen, 1996; Haboudane et al., 2004
NDVI	Normalized Difference Vegetation Index	$(R_{NIR}-R_R)/(R_{NIR}+R_R)$, where R_{NIR} indicates 775-825nm, R_R indicates 650nm-700nm, that include most key pigments	Rouse et al., 1973
NBNDVI	Narrow-band normalised difference vegetation index	$(R_{850}-R_{680})/(R_{850}+R_{680})$	Thenkabail et al., 2000
NRI	Nitrogen reflectance index	$(R_{570}-R_{670})/(R_{570}+R_{670})$	Filella et al., 1995
PRI	Photochemical Physiological Reflectance Index	$(R_{531}-R_{570})/(R_{531}+R_{570})$	Gamon et al., 1992
TCARI	The transformed chlorophyll Absorption and Reflectance Index	$3*[(R_{700}-R_{670})-0.2*(R_{700}-R_{550})*(R_{700}/R_{670})]$	Haboudane et al., 2002
SIPI	Structural Independent Pigment Index	$(R_{800}-R_{445})/(R_{800}-R_{680})$	Peñuelas et al., 1995
PSRI	Plant Senescence Reflectance Index	$(R_{680}-R_{500})/R_{750}$	Merzlyak et al., 1999
PhRI	The Physiological reflectance index	$(R_{550}-R_{531})/(R_{550}+R_{531})$	Gamon et al., 1992
NPCI	Normalized Pigment Chlorophyll ratio Index	$(R_{680}-R_{430})/(R_{680}+R_{430})$	Peñuelas et al., 1994
ARI	Anthocyanin Reflectance Index	$ARI=(R_{550})^{-1}-(R_{700})^{-1}$	Gitelson et al., 2001
TVI	Triangular Vegetation Index	$0.5[120(R_{750}-R_{550})-200(R_{670}-R_{550})]$	Broge and Leblanc, 2000; Haboudane et al., 2004
CARI	Chlorophyll Absorption Ratio Index	$(\lvert(a670+R_{670}+b)\rvert/(a^2+1)^{1/2})x(R_{700}/R_{670})$ $a = (R_{700}-R_{550})/150$, $b = R_{550}-(a \times 550)$	Kim et al., 1994

Variable	Definition	Description	Literatures
DSWI	Disease Water Stress Index	$(R_{802}+R_{547})/(R_{1657}+R_{682})$	Galvão et al., 2005
MSI	Moisture Stress Index	R_{1600}/R_{819}	Hunt and rock, 1989; Ceccato et al., 2001
SIWSI	Shortwave Infrared Water Stress Index	$(R_{860}-R_{1640})/(R_{860}+R_{1640})$	Fensholt and Sandholt, 2003
RVSI	Red-Edge Vegetation Stress Index	$[(R_{712}+R_{752})/2]-R_{732}$	Merton and Huntington, 1999
MCARI	Modified Chlorophyll Absorption in Reflectance Index	$(R_{701}-R_{671})-0.2(R_{701}-R_{549})]/(R_{701}/R_{671})$	Daughry et al., 2000
WI	Water Index	R_{900}/R_{970}	Peñuelas et al., 1997

Table 2. Definitions of spectral features used in this study

2.1.1.4 Preprocessing and normalization of spectral reflectance data

Aggregating spectral reflectance data

As the first step, all spectra were processed with the following transformation to suppress possible difference in illumination. The spectral regions with wavelength of 1330-1450 nm, 1770-2000 nm and 2400-2500 nm were removed due to strong absorption by water vapor. We then normalized the spectral curves by dividing the mean band reflectance of the curve (Yu et al., 1999). The normalized reflectance for the $band_i$ is given as:

$$Ref_i' = \frac{Ref_i}{\frac{1}{n}(\sum_{i=1}^{n} Ref_i)}$$

where Ref_i' is the normalized reflectance for $band_i$; Ref_i is the original reflectance of the band; n is the total number of bands. Fig. 1(a) shows a plot of unnormalized Ref_i versus band wavelength for six observations (three YR3 curves and three Normal curves) on 233 DAS. Fig. 1(b) shows the corresponding curves in Fig.1(a) after normalization. The normalization clearly separated the diseased spectra from the normal spectra especially over the near infrared region (approximately from 770 nm to 1300 nm). The benefit of eliminating spectral difference caused by the change of illumination conditions was also mentioned by Yu et al. (1999).

Normalization of the difference in measuring dates

As shown in Table 1, although both experiments conducted in five growth stages in 2002 and 2003, most measurement dates were not consistent, except for 255 DAS. Hence, to improve the comparability of two datasets, we adapted the 2002 Exp data to match the dates

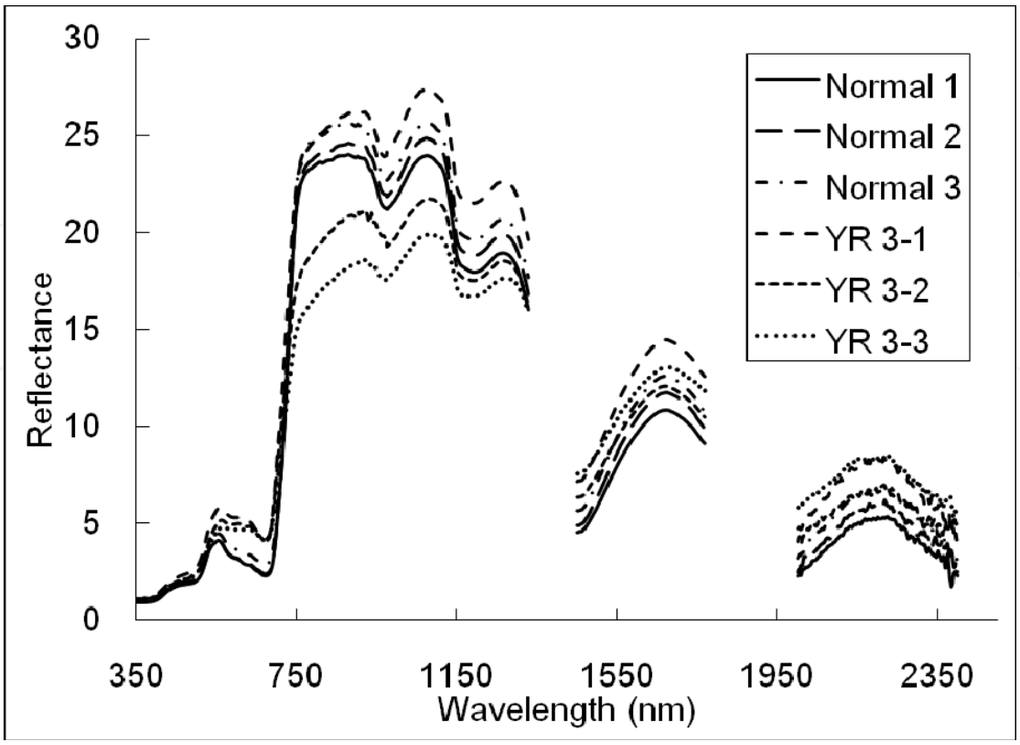

(a) Original spectra on 233 days after sowing

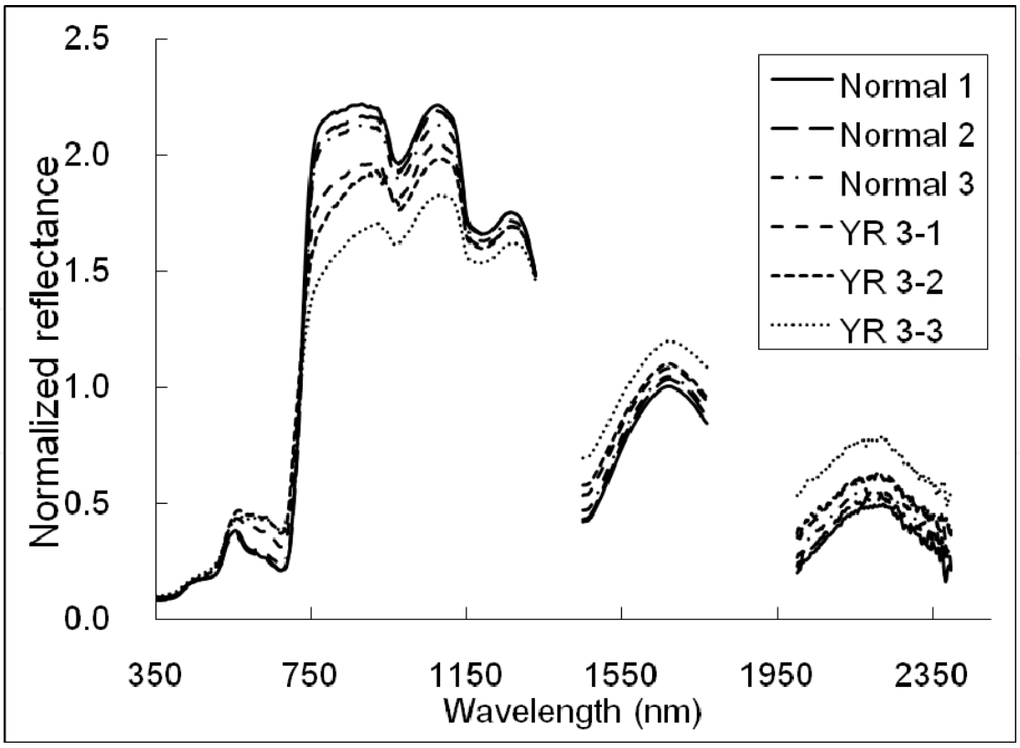

(b) Normalized spectra on 233 days after sowing

Fig. 1. Comparison between original spectra and normalized ones

of 2003 Exp, by using a linear interpolation method. The reflectance curve of a certain date could be obtained based on the spectra from the adjacent data before and after the measurement date (using days after sowing as a time scale). Each band of the spectra should be processed as:

$$Ref_{current} = Ref_{before} - \frac{DAS_{current} - DAS_{before}}{DAS_{after} - DAS_{before}}(Ref_{before} - Ref_{after})$$

where $Ref_{current}$ represents the reflectance transformed from the date corresponding to an ideal date in 2003 Exp; Ref_{before} and Ref_{after} represent reflectances, respectively, from DAS_{before} and DAS_{after}; $DAS_{current}$ indicates an ideal date in 2003 Exp while DAS_{before} and DAS_{after} are the adjacent dates in 2002 Exp before and after the ideal date in 2003 Exp.

Fig. 2 provides an example of the progress of the normalization of measurement dates. The averaged reflectance at central wavelengths of green band (560 nm) and near-infrared band (860 nm) of Landsat-5 TM for normal samples were plotted against the measured dates in both 2002 Exp and 2003 Exp. The date normalized reflectance values were marked as triangle symbol in the graph. Through this step, the datasets collected in these two years could be considered as acquired in the same dates, which thereby facilitated the subsequent comparisons and analysis.

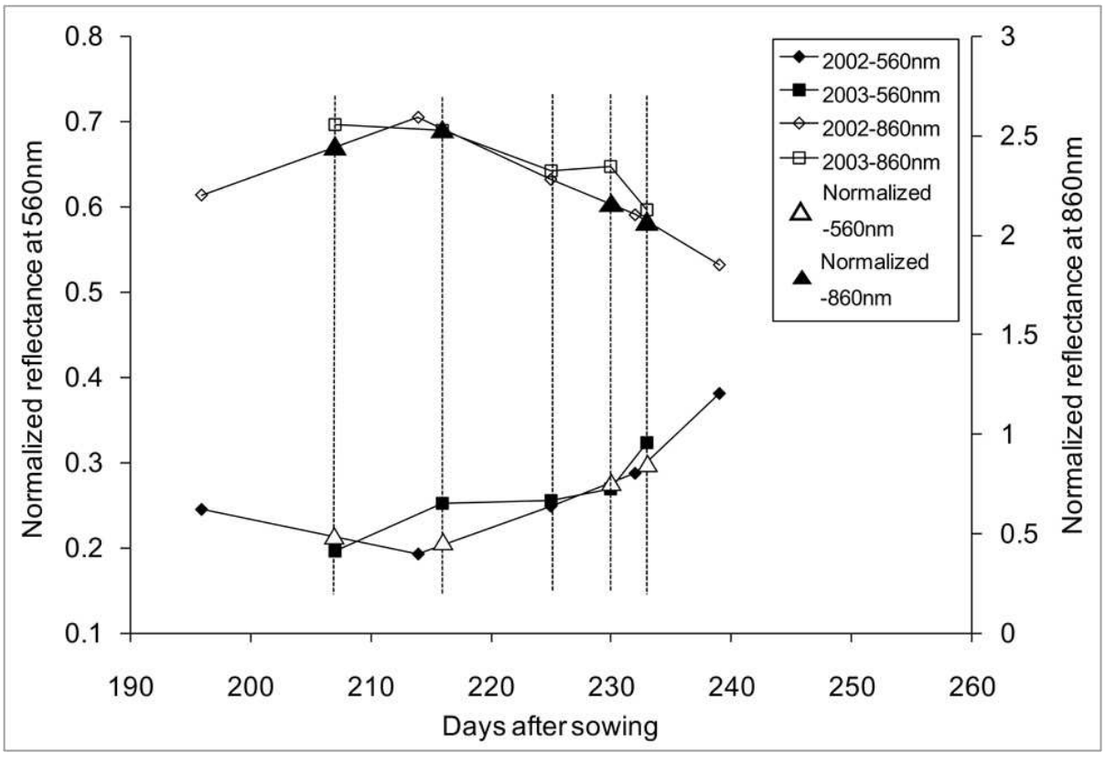

Adaptation of average reflectance of normal samples at 560 nm (central wavelengths of green band of Landsat-5 TM) and 860 nm (central wavelengths of near-infrared band of Landsat-5 TM) to match the dates of 2003 Exp, by using a linear interpolation method

Fig. 2. An example for normalization of measuring dates

Normalization of the difference from cultivars and soil backgrounds

The canopy spectra of winter wheat were not only supposed to respond to stresses, but are also determined and influenced by several other aspects such as cultivars and soil properties. Although the both 2002 Exp and 2003 Exp were conducted in the same fields that had approximately identical climate and environmental conditions, the difference in cultivars and soil properties between 2002 Exp and 2003 Exp should not be ignored (Table 1). To minimize this discrepancy, we calculated a ratio spectral curve for each of measured dates (after the normalization of the measuring dates) by the averaged spectral curve from normal samples in 2002 Exp divided by the averaged spectral curve from normal samples in 2003 Exp, resulting in a total of five ratio curves corresponding to each growth stage (Fig. 3). After that, all the spectral data measured at different growth stages were multiplied by the corresponding ratio curves to yield a set of normalized spectra. It should be pointed out that the present normalization processing to raw spectral measurements will only enhance the comparability between the 2002 Exp and 2003 Exp with little change in internal relations among different treatments because all the spectral data at one growth stage were processed with the same ratio curve. The ultimate goal of all these preprocessing and normalization steps above is to mitigate effects of the variation of illumination conditions, measurement dates, cultivars and soil properties between the 2002 Exp and 2003 Exp on target spectra.

2.1.1.5 Spectral features calculation and statistical analysis

With the spectra normalized using the methods above, we calculated 38 spectral features. An analysis of variance (ANOVA) was employed to investigate the spectral differences between the normal samples and all forms of stressed samples. Firstly, on different measured dates, both the yellow rust disease data and nutrient stressed data were compared with the normal data by ANOVA. For those spectral features that were consistently sensitive to yellow rust disease, we not only tested their differences between the normal treatment and different forms of stresses, but also tested the differences between various kinds of nutrient stresses and varying levels of disease stresses with ANOVA. Statistical analyses were conducted using SPSS 13.0 procedure.

2.1.2 Results

2.1.2.1 Spectra after normalizations

The spectral ratio curves in Fig 3 reflect the deviations between 2002 Exp and 2003 Exp's reflectance datasets at different wavelength positions. The ratio value close to 1.0 indicates no difference in reflectance exists between the two years. Generally, the ratio values ranged from 0.7 to 1.3, with an uneven distribution along the wavelength axis (Fig 3). The ratio tended to deviate from 1.0 in the regions of 350 - 730 nm, 1450 - 1570 and 2000 - 2400 nm, but stayed around 1.0 in the regions of 730 - 1330 nm and 1570 - 1770 nm. To assess the improvement in comparability, we examined the difference of normalized datasets of normal samples between 2002 Exp and 2003 Exp through an ANOVA with all 38 spectral features. The result showed that the differences of all spectral features were insignificant at all growth stages (p-value>0.05), with an average p-value (for all measuring dates) of 0.94, indicating a relatively high level of similarity between two datasets. Therefore, we confirmed that such normalization processes minimized the spectral difference originated

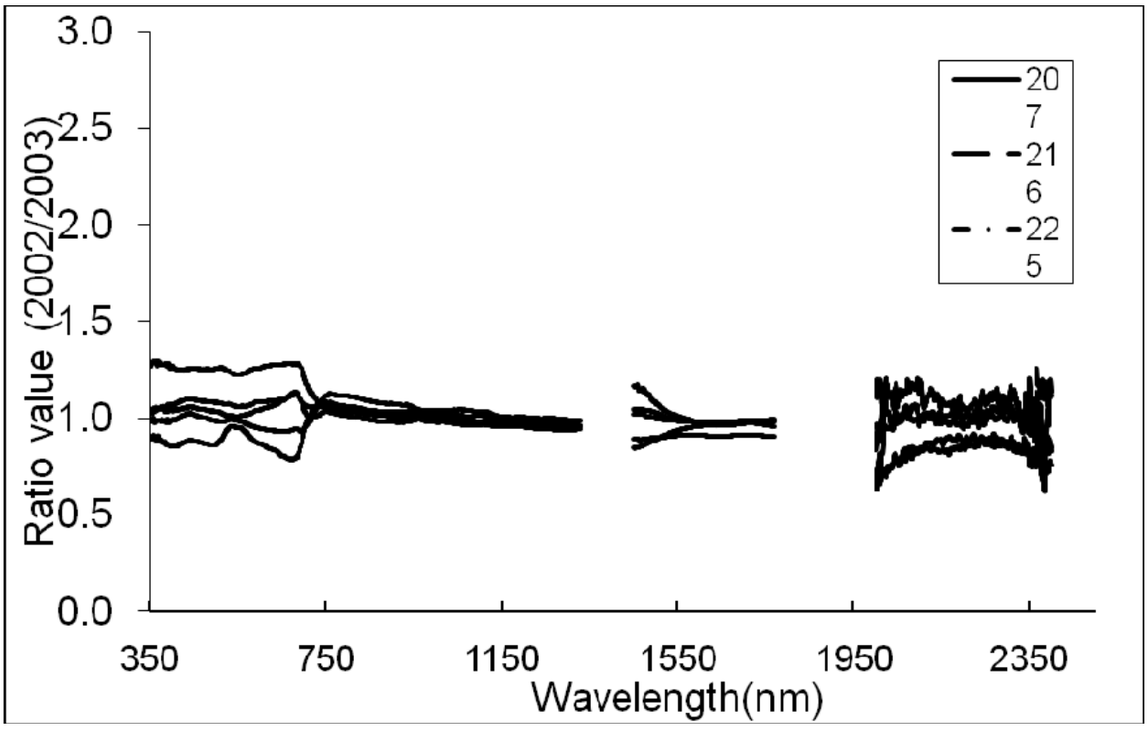

Fig. 3. Ratios of spectra for normalization with different years and varieties

from variation of illumination and different measurement dates, etc., and enabled more rational comparisons among different treatments.

2.1.2.2 Spectral responses to different forms of stresses

The result of ANOVA between normal samples and different forms of stress samples indicated that all spectral features had a response (defined as *p*-value<0.05) to at least one type of stresses at one growth stage, except for the WID1070-1320, which had no response to any form of stresses at all growth stages. Total 37 spectral features responded to water associated stresses (W-SD, W-SED, W-SED+N-E, W-SED+N-D) at least at one growth stage, followed by 35 spectral features to yellow rust disease, whereas only15 spectral features had a response to solely nitrogen stress (N-E, N-D). As summarized in Table 3, most spectral features were sensitive to yellow rust infection at least at one growth stage, except for λ_b, λ_r and WID1070-1320. In addition, most spectral features tended to be more sensitive at later growth stages than at the early stages. For example, several features such as DEP920-1120, AREA920-1120, D_y, GI, NDVI and Triangular Vegetation Index (TVI) only had a response to yellow rust at the last growth stage in our study (233 DAS). However, for the sake of diagnosis, the spectral features with a consistent response to yellow rust during the important growing period would be much more valuable. Therefore, those spectral features that were sensitive to the yellow rust at 4 out of 5 growth stages were selected as candidates for disease diagnosis. This yielded four vegetation indices (VIs): PRI, PhRI, NPCI and ARI.

2.1.2.3 One way ANOVA of four disease sensitive spectral features

Particularly for the four identified VIs that closely associated with yellow rust disease, a throughout one way ANOVA was conducted to compare their differences between the

Spectral features	Days after sowing				
	207	216	225	230	233
DEP550-770	√			√	√
AREA550-770	√			√	√
WID550-770			√	√	√
DEP920-1120					√
AREA920-1120					√
WID920-1120					√
DEP1070-1320					√
AREA1070-1320					√
Db			√	√	
SDb			√	√	√
Dy					√
λy					√
SDy					√
Dr				√	
SDr				√	√
GI					√
MSR				√	√
NDVI					√
NBNDVI				√	√
NRI					√
PRI		√	√	√	√
TCARI			√	√	
SIPI					√
PSRI	√			√	√
PhRI		√	√	√	√
NPCI	√		√	√	√
ARI	√		√	√	√
TVI					√
CARI			√	√	√
DSWI					√
MSI					√
SIWSI					√
RVSI			√	√	
MCARI			√	√	√
WI					√

Table 3. Responses of spectral features to yellow rust

normal sample and various kinds of stressed samples. Moreover, their differences among each pairs of stress forms were also compared. We conducted this ANOVA based on the data on 207 DAS, 225 DAS and 233 DAS respectively, which were essential growth stages for carrying out fungicide spraying and yield loss assessing procedures. In addition to the *p*-value of ANOVA, we also provided the change direction of spectral features. Positive sign indicates the average spectral feature value of diseased or nutrient stressed samples is greater than that of normal samples, and negative sign indicates the opposite cases to the positive sign. As shown in Table 4, it was observed that for the treatments of N-E and N-D, all four VIs failed to show any response at all growth stages. For the results of other treatments, the responses of four VIs behaved in a varied pattern at three growth stages.

For the results on 207 DAS (Table 4a), compared to the normal samples, the NPCI and ARI had responses to all three levels of yellow rust treatments (YR 1, YR 2, YR 3), and appeared to be more sensitive than PRI and PhRI. For nutrient stresses, the PRI, NPCI and ARI were sensitive to W-SED and W-SED+N-E treatments. Among them, NPCI and ARI showed stronger responses (p-value<0.01) to W-SD, W-SED, W-SED+N-E and W-SED+N-D treatments than the other two VIs. For the comparisons between diseased samples and nutrient stressed samples, significant differences between W-SED and W-SED+N-E treatments and YR2 and YR3 treatments were identified for PRI, NPCI and ARI. Moreover, the change directions of the three VIs for diseased and nutrient stressed samples were identical. At this 207 DAS growth stage, PhRI did not show a significant response to any of three levels of disease treatments, but responded to W-SD, W-SED and W-SED+N-E treatments. It is interesting that the change direction of diseased samples of PhRI was contrary to that of the nutrient stressed samples, suggesting a discriminating potential of the index.

For the results on 225 DAS (Table 4b), compared to the normal samples, all four VIs revealed a clear response to level 2 and level 3 of yellow rust treatments (YR2, YR3). For nutrient stresses, PRI, NPCI and ARI also appeared to be sensitive to W-SD, W-SED, W-SED+N-E and W-SED+N-D treatments. However, PhRI was insensitive to all nutrient stresses. In addition, when we looked at the difference of those VIs between diseased samples and nutrient stressed samples, only PhRI showed clear differences between YR2 and YR3 treatments and W-SD, W-SED, W-SED+N-E, and W-SED+N-D treatments. Although a significant difference between YR3 treatment and W-SED treatment also existed for ARI and NPCI, the change directions of both treatments were identical. However, for PhRI, the change directions of all levels of disease treatments were different from those of the nutrient stress treatments.

For the results on 233 DAS (Table 4c), with further development of disease symptoms, compared to the normal samples, all four indices showed responses to all three levels of disease treatments. Comparing to YR1 treatment, the four VIs had shown a stronger significant level (p-value<0.01) for YR2, YR3 treatments. For nutrient stresses, PRI, NPCI and ARI exhibited clear responses to W-SED, W-SED+N-E and W-SED+N-D treatments as well. For comparisons between diseased and nutrient stressed samples, PRI and NPCI appeared to be significantly different between YR2 and YR3 treatments and W-SD treatment. However, the change directions of both treatments were identical. Unlike the other three VIs, PhRI remained insensitive to the nutrient stresses, but was significantly different among all levels of disease treatments (YR1, YR2, and YR3) and all forms of nutrient stresses. More

Treatments	YR 1				YR 2				YR 3				Normal			
	PRI	PhRI	NPCI	ARI	PRI	PhRI	NPCI	ARI	PRI	PhRI	NPCI	ARI	PRI	PhRI	NPCI	ARI
Normal	(-)	(-)	(+) *	(-) *	(-) *	(+)	(+) *	(-) *	(-)	(+)	(+) **	(-) ***				
W-SD	(-)	(-)	(+)	(+)	(-)	(-) *	(+)	(+)	(-)	(-) *	(+)	(-)	(-)	(-) *	(+) **	(-) **
W-SED	(+)	(-)	(+) *	(+) *	(+)	(-) *	(+) *	(+) *	(+) *	(-) *	(+) *	(+)	(-) ***	(-) *	(+) ***	(-) ***
N-E	(-)	(+)	(-)	(-)	(-) *	(-)	(-)	(-)	(-)	(-)	(-) *	(-) **	(+)	(-)	(-)	(+)
N-D	(-)	(+)	(-)	(-)	(-)	(+)	(-)	(-)	(-)	(-)	(-) *	(-) **	(-)	(+)	(-)	(+)
W-SED+N-E	(+)	(-)	(+) *	(+) *	(+)	(-) *	(+) *	(+) *	(+) *	(-) *	(+)	(+)	(-) ***	(-) *	(+) ***	(-) ***
W-SED+N-D	(+)	(-)	(+)	(+)	(+)	(-)	(+)	(+)	(+)	(-) *	(+)	(+)	(-) *	(-)	(+) **	(-) ***

(a) 207 DAS

Treatments	YR 1				YR 2				YR 3				Normal			
	PRI	PhRI	NPCI	ARI	PRI	PhRI	NPCI	ARI	PRI	PhRI	NPCI	ARI	PRI	PhRI	NPCI	ARI
Normal	(+)	(+)	(+)	(+)	(+) **	(+) ***	(+) *	(+) *	(+) ***	(+) ***	(+) **	(+) **				
W-SD	(+) **	(-) *	(+) **	(+) **	(-)	(-) **	(+)	(+)	(-)	(-) **	(+)	(+)	(+) ***	(-)	(+) ***	(+) **
W-SED	(+) **	(-)	(+) ***	(+) **	(-)	(-) **	(+)	(+)	(+)	(-) *	(+) **	(+) **	(+) ***	(-)	(+) ***	(+) ***
N-E	(-) *	(-)	(-)	(-)	(-) *	(-) *	(-)	(-)	(-) *	(-) *	(-) *	(-) **	(-)	(-)	(-)	(-)
N-D	(-)	(+)	(-)	(-)	(-)	(-) *	(-)	(-)	(-) *	(-) *	(-) *	(-) **	(+)	(+)	(+)	(-)
W-SED+N-E	(+) *	(-)	(+) *	(+) *	(-)	(-) **	(+)	(+)	(-)	(-) *	(+)	(+)	(+) ***	(-)	(+) ***	(+) **
W-SED+N-D	(+) *	(-)	(+) *	(+) *	(-)	(-) **	(+)	(+)	(-)	(-) *	(+)	(+)	(+) ***	(-)	(+) **	(+) **

(b) 225 DAS

Treatments	YR 1				YR 2				YR 3				Normal			
	PRI	PhRI	NPCI	ARI	PRI	PhRI	NPCI	ARI	PRI	PhRI	NPCI	ARI	PRI	PhRI	NPCI	ARI
Normal	(+) **	(+) *	(+) *	(+) *	(+) ***	(+) **	(+) ***	(+) ***	(+) ***	(+) **	(+) ***	(+) ***				
W-SD	(-)	(-) **	(-)	(+)	(-) ***	(-) **	(-) *	(-)	(-) **	(-) **	(-) **	(-) *	(+)	(-)	(+) *	(+) *
W-SED	(+)	(-) **	(+)	(+)	(-) *	(-) **	(+)	(-)	(-) *	(-) **	(-)	(-)	(+) ***	(-)	(+) ***	(+) ***
N-E	(-) *	(-) **	(-)	(-)	(-) ***	(-) **	(-) **	(-) *	(-) ***	(-) **	(-) ***	(-) **	(-)	(-)	(-)	(+)
N-D	(-) *	(-) *	(-)	(-)	(-) ***	(-) **	(-) **	(-) *	(-) ***	(-) **	(-) **	(-) **	(-)	(-)	(+)	(+)
W-SED+N-E	(+)	(-) **	(+)	(+)	(-) **	(-) **	(+)	(+)	(-) *	(-) **	(-)	(+)	(+) ***	(-)	(+) ***	(+) ***
W-SED+N-D	(+)	(-) **	(+)	(+)	(-) ***	(-) **	(+)	(-)	(-) *	(-) **	(-)	(-)	(+) ***	(-)	(+) ***	(+) ***

(c) 233 DAS

*mean difference is significant at 0.950 confidence level; **mean difference is significant at 0.990 confidence level;*** mean difference is significant at 0.999 confidence level. (+) means the average spectral feature value of diseased or nutrient stressed samples greater than that of normal samples; or means the average spectral feature value of nutrient stressed samples greater than that of diseased samples; (-) means the opposite cases to the case of (+). The definitions of treatments are as follows: "Normal" represents normal samples; "W-SD" represents samples treated with slightly deficient water; "W-SED" represents samples treated with seriously deficient water; "N-E" represents samples treated with excessive nitrogen; "N-D" represents samples treated with deficient nitrogen; "W-SED+N-E" represents samples treated with seriously deficient water and excessive nitrogen; "W-SED+N-D" represents samples treated with seriously deficient water and deficient nitrogen

Table 4. ANOVA for four VIs separately on 207 DAS, 225 DAS and 233 DAS

importantly for the PhRI, the change directions of diseased samples were opposite to those of nutrient stressed samples throughout the entire analysis.

In summary, all four VIs showed a significant sensitivity to yellow rust disease on 207 DAS, 225 DAS and 233 DAS. However, most of them also appeared to be sensitive to water associated stresses to a varing extent, except for PhRI, which was only sensitive to disease yet insensitive to any forms of nutrient stresses on 225 DAS and 233 DAS. More importantly, the change directions of PhRI to disease treatments were always opposite to those to the nutrient stress treatments at all relevant growth stages. This further confirmed the discriminating characteristic of PhRI.

2.1.3 Conclusion

Combining with a dataset of yellow rust disease inoculation and a dataset of various forms of nutrient stress treatments, we examined the responses of 38 commonly used spectral features at five important growth stages from booting stage to milk development stage using a one-way analysis of variance (ANOVA). There were 37 spectral features sensitive to water associated stresses, 35 spectral features sensitive to yellow rust disease and only 15 spectral features sensitive to sole nitrogen stresses in at least one growth stage. It was observed that more spectral features appeared to have a response to yellow rust disease at later growth stages. A throughout ANOVA was conducted particularly on PRI, PhRI, NPCI and ARI, which showed a consistent response to yellow rust disease at 4 out of 5 growth stages. However, PRI, NPCI and ARI were also responsible for water associated stresses, suggesting a risk of confusion in detecting yellow rust disease. Only PhRI was sensitive to yellow rust disease, but insensitive to different forms of nutrient stresses. The discriminative response of PhRI could provide a means of identifying and detecting yellow rust disease under complicated farmland circumstances. This finding can serve the basis of remote sensing system for detecting yellow rust disease.

2.2 Detecting yellow rust using field and airborne hyperspectral data

The aim of this study was to evaluate the accuracy of the spectro-optical, photochemical reflectance index (PRI) for quantifying the disease index (DI) of yellow rust in wheat using in-situ spectral reflectance measurements, and its applicability in the detection of the disease using hyperspectral imagery.

2.2.1 Materials and methods

2.2.1.1 Experimental design and field conditions

Experimental design and field conditions was same as 1.1.1. Experimental data from 2002 Exp were used to establish the statistical models, and the data for 2003 Exp were used to validate the models developed.

2.2.1.2 Inspection of disease severity

To quantify the severity of the disease of yellow rust, the leaves of plants were grouped into one of 9 classifications of disease incidence (x): 0,1, 10, 20, 30, 45, 60, 80 and 100% covered by rust. 0% represented no incidence of yellow rust, and 100% was the greatest incidence. The disease index (DI) was then calculated using (Li et al. 1989):

$$DI(\%) = \frac{\sum(x \times f)}{n \times \sum f} \times 100$$

where f is the total number of leaves of each degree of disease severity and n is the degree of disease severity observed (in this work, n ranged from 0 to 8). In each plot, 20 individuals were randomly selected for check.

2.2.1.3 Canopy spectral measurements

The method of canopy spectral measurements and data was same as the part 1.1.1.2 above.

2.2.1.4 Airborne hyperspectral imaging

Airborne hyperspectral images of the trial field were acquired in 2003 using the Pushbroom Hyperspectral Imager (PHI) designed by the Chinese Academy of Science (CAS) and flown onboard a Yun-5 aircraft (Shijiazhuang Aircraft Manufacturing Company, China). The PHI comprises a solid state, area array, and silicon CCD device of 780 × 244 elements. It has a field of view of 21°, and is capable of acquiring images of 1 m × 1 m spatial resolution at an altitude of 1000 m above ground. The wavelength range is 400–850 nm with a spectral resolution of 5 nm. Images of the target field were acquired in 2003 at the phenological growth stages of stem elongation (April 18, 2003, Zadoks stage 3), anthesis (May 17, 2003, Zadoks stage 5) and milky maturity (May 31, 2003, Zadoks stage 8). The inoculated wheat was adequately infected by rust on April 18, obviously infected by May 17, and seriously infected by May 31. Measurements of DI were made and in situ canopy reflectance spectra were also acquired on the same dates. All images were geometrically and radiometrically corrected using an array of georeferenced light and dark targets (5 m x 5 m) located at the extremes of the field site. The aforementioned field spectrometer was used to calibrate these targets relative to BaSO4. The location of each target, as well as field measurements of DI were recorded using a differential global positioning system (Trimble Sunnyvale California, USA).

2.2.1.5 Photochemical reflectance index (PRI)

Because yellow rust epiphyte reduced foliar physiological activity by destroying foliar pigments, the photochemical reflectance index (PRI) was selected as the spectrophotometric method of estimating the disease index. PRI was calculated by the formula in Table 2.

2.2.2 Results

2.2.2.1 PRI versus DI

Fig. 4 shows a plot of the measured DI as a function of PRI for all varieties. The data points associated with the variety Xuezao dominate in the top-left region of the scatter plot (relatively high range of DI), while those associated with the variety 98-100 are located in the mid region (mid-range DI) and those associated with Jing 411 dominate the lower right region. This distribution trend is consistent with the relative susceptibility of these varieties to rust; Xuezao is the least resistant and Jing 411 has the greatest resistance. The regression equation of DI using PRI in 2002 Exp was obtained as following (n = 64):

$$\mathrm{DI}(\%) = -721.22(PRI) + 2.40 \qquad \left(-0.14 \le PRI \le 0.02; r^2 = 0.91\right)$$

An important feature in, the associated regression equation (Fig. 4) was that the spectrally-derived PRI explained 91% of the variance observed in the disease index. This explanation also encompassed the three varieties of wheat as well as the four stages of crop development for each variety. In the subsequent validation of the PRI-DI regression equation with the 2003 Exp data (Fig. 5), the coefficient of determination (R^2) between the estimated and measured values was 0.97 (n = 80).

In Fig. 5, the locations of data points associated with individual varieties wew consistent with the levels of resistance to rust. Xuezao dominated the top right-hand region of the scatter plot (relatively high range of DI), the variety 98-100 had points scattered all along the

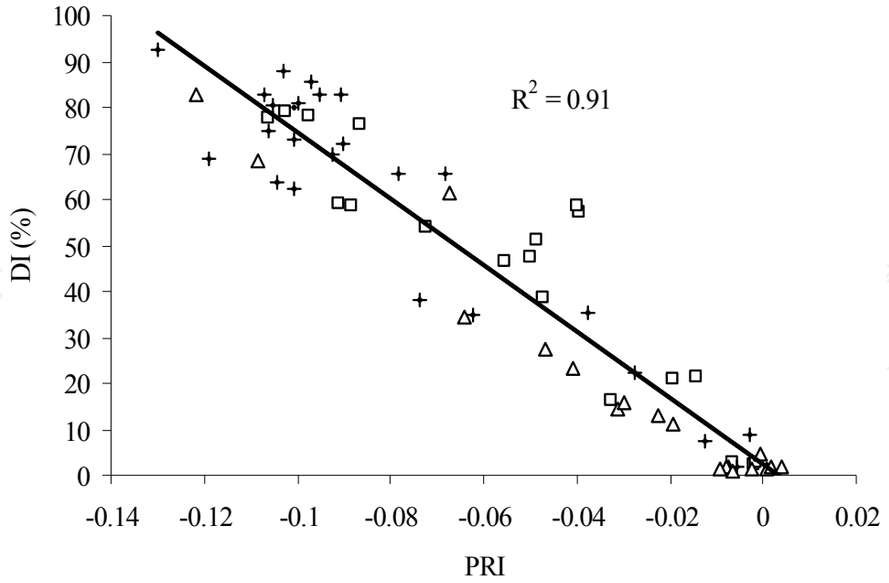

Fig. 4. Plot of measured disease index (DI) as a function of measured photochemical reflectance index(PRI) for all varieties combined in 2002 Exp. Δ: Jing 411; +: Xuezao; □: 98–100

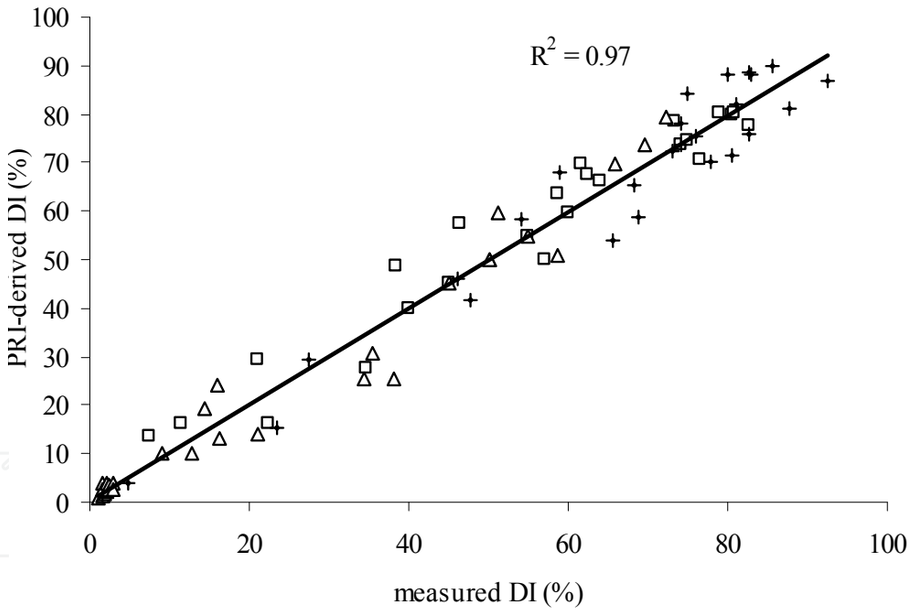

Fig. 5. Comparison of measured DI and PRI-estimated DI for 2003 Exp; 'Δ' = Jing 411; '+' = Xuezao; '□' = 98–100

regression line (predominantly mid-range DI), and Jing 411 was concentrated in the central lower-left region (lower range DI).

2.2.2.2 Application of multi-temporal PHI images for DI estimation

The DI was estimated on a pixel-by-pixel basis in each of the acquired PHI images using the regression equation. To map the degree of yellow rust infection in the trial field, the DI was

binned into the following classes; very Serious (DI > 80%), serious (45% < DI ≤ 80%), moderate (10% < DI ≤ 45%), slight (1% < DI ≤ 10%) and none (0 < DI ≤ 1%) (Fig. 6).

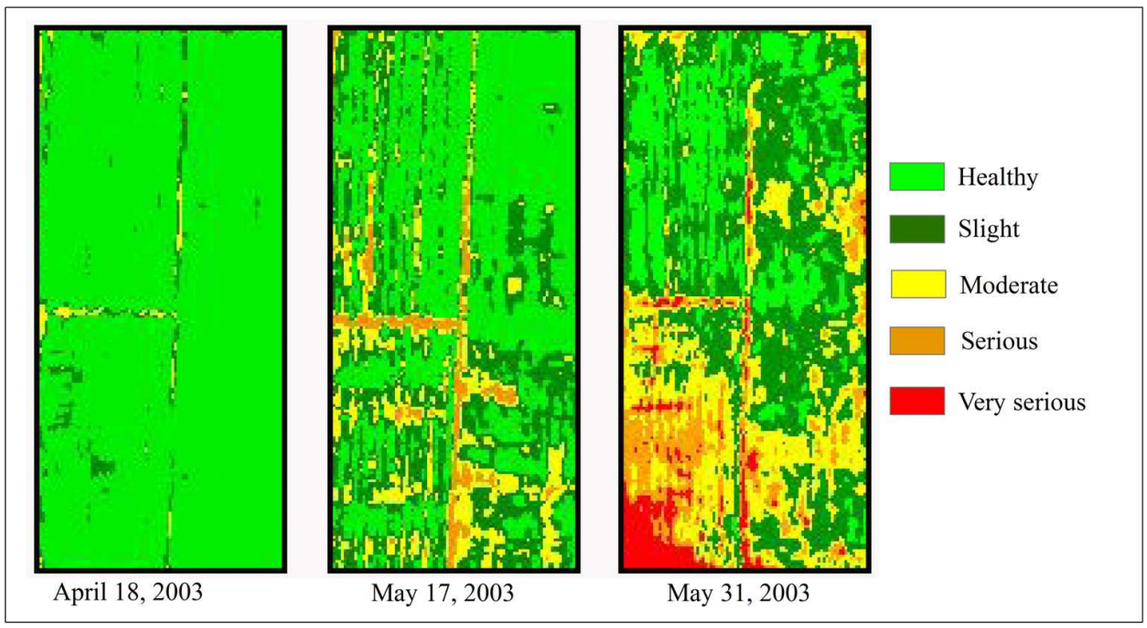

Fig. 6. Classified DI images derived from PHI airborne images of the trial site in 2003 Exp

Fig. 7 shows the relationship between the DI calculated from the multi-temporal PHI images and the actual measured DI from the 120 sample sites located within the field (R^2=0.91).

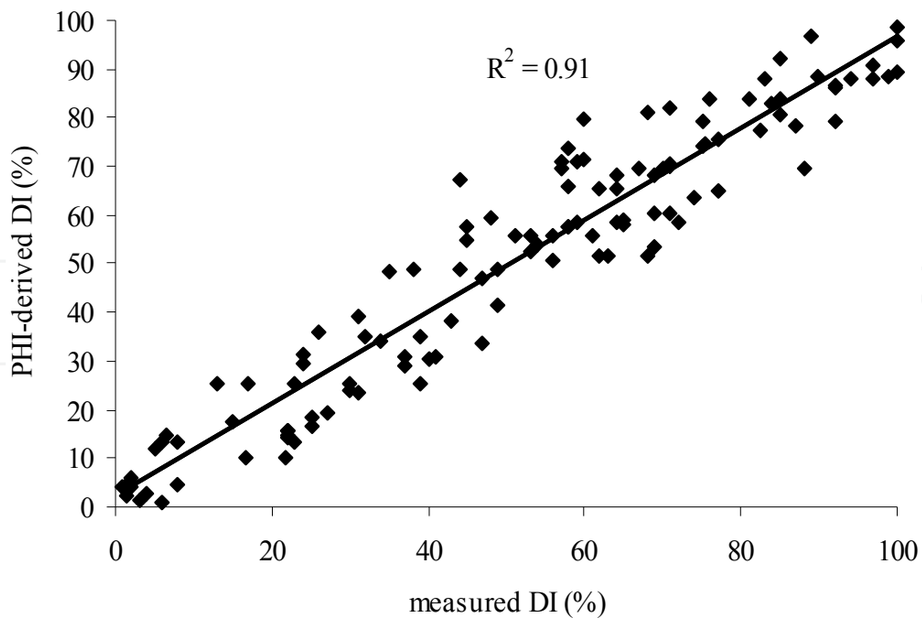

Fig. 7. Comparison of PHI-derived estimates of DI and actual DI values for 2002 Exp. Data were extracted from all three imaging times, although the DI values were< 20% for the April 18 image

2.2.3 Conclusion

The results of this work confirm PRI is a potential candidate for monitoring of yellow rust, and could form the basis of an on-the-go sensor and variable-rate spray applicator or remote detection and mapping process.

2.3 Detecting yellow rust in winter wheat by spectral knowledge base

In most cases, statistical models for monitoring the disease severity of yellow rust are based on hyperspectral information. The high cost and limited cover of airborne hyperspectral data make it impossible to apply such data for large scale monitoring. Furthermore, the established models of disease detection cannot be used for most satellite images because of the wide range of wavelengths in multispectral images (Zhang et al., 2011).

To resolve this dilemma, the study presents a novel approach by constructing a spectral knowledge base (SKB) of winter wheat diseases, which takes the airborne images as a medium and links the disease severity with band reflectance from moderate resolution remotely sensed data, such as environment and disaster reduction small satellite images (HJ-CCD) accordingly. To achieve this goal, several algorithms and techniques for data conversion and matching are adopted in the proposed system, including minimum noise fraction (MNF) transformation and pixel purity index (PPI) function. The performance of SKB is evaluated with both simulated data and field measured data.

2.3.1 materials and methods

Experimental design and field conditions was same as the part of 1.1.1.1

2.3.1.1 Inspection of disease severity

Please refer to the part of 1.2.1.2 above.

2.3.1.2 Airborne hyperspectral imaging

Please refer to the part of 1.2.1.4 above about airborne hyperspectral imaging and image processing.

2.3.1.3 Acquisition of moderate resolution satellite images

In this study, the SKB is designed to fit the charge coupled device (CCD) sensor, which is on the environment and disaster reduction small satellites (HJ-1A/B). The basic parameters of the CCD sensor (using 'HJ-CCD' in the following) are given in Table.5. The four bands of

	Properties of HJ-CCD			
Band	Wavelength range (nm)	Spatial resolution (m)	Swath (km)	Revisit time (day)
Blue	0.430–0.520	30	360	2
Green	0.520–0.600			
Red	0.630–0.690			
Near-infrared	0.760–0.900			

Table 5. Properties of the environment and disaster reduction small satellites (HJ-CCD)

HJ-CCD covered the visible and near infrared spectral regions. The HJ-CCD sensor has spectral and spatial characteristics that are similar to those of Landsat-5 TM, but the HJ-1A/B satellites have more frequent revisit capability (2 days) than the Landsat-5 satellite (16 days), which is of great importance for agricultural monitoring.

2.3.1.4 Construction of the spectral knowledge base

The SKB in this study can be interpreted as a pool of relationships between spectral characteristics and prior knowledge. Here, prior knowledge stands for the degree of severity of yellow rust, and the spectral characteristics are the reflectance of the initial four bands of the HJ-CCD image. Hence, there are two major steps involved in constructing the SKB. First, the relationship between hyperspectral information and severity is obtained with a stable empirical reversion model. Then, through the RSR function of the HJ-CCD sensor, the hyperspectal data can be transferred to the wide-band reflectance. In this way, a one-to-one correspondence between the disease severity of yellow rust and reflectances from the HJ-CCD sensor is established at the pixel level. The SKB can represent disease severity in two ways: the DI (%) value and the class of disease severity. The following sections describe each step for establishing the SKB, including data selection, the reversion model, simulation of the wide-band reflectance and estimating the degree of severity. A technical flow diagram of SKB construction is summarized in Fig. 8.

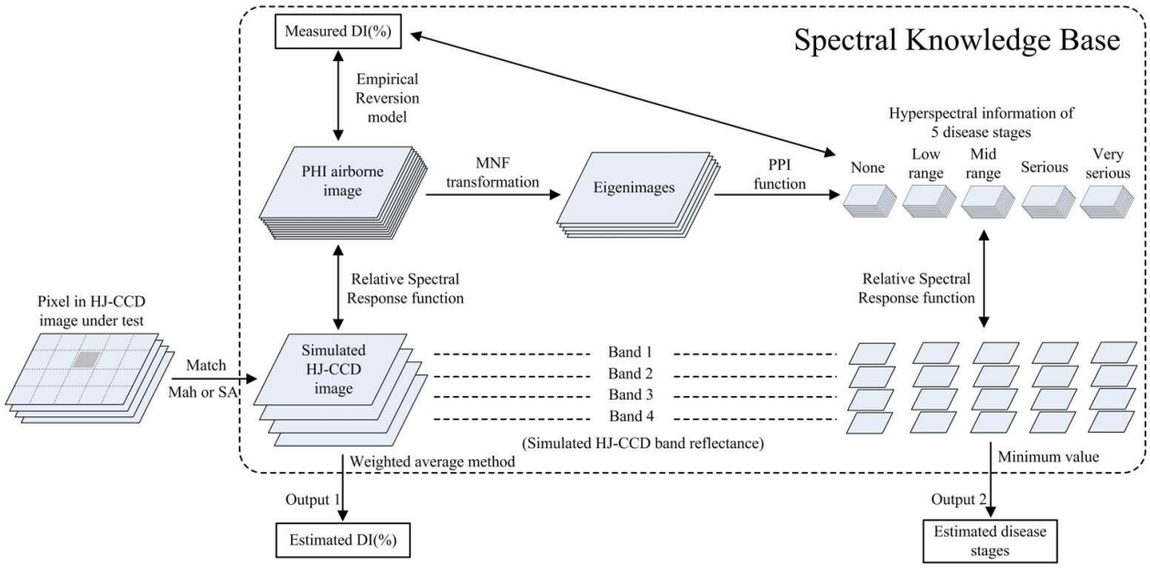

Fig. 8. The flow chart for monitoring of DI(%) of winter wheat stripe rust, b1-b4 represented the reflectance of the four bands of HJ-CCD images

As noted above, the SKB in this study comprised PHI pixels. The predicted accuracy obtained by the SKB was determined primarily by the amount of prior knowledge, which indicated the heterogeneity of disease severity. The design of the yellow rust fungus inoculation ensured a considerable variation in disease severity within the experimental field, from healthy plants to very diseased plants. In addition, to avoid using pixels on or near the ridge in the field that are considered as mixed signals, we chose three rectangular

shaped areas that were within the field and comprised 7918 'crop-only' pixels for constructing the SKB.

2.3.1.5 Reversion model

The reversion model construction was the first step of establishing the SKB. Based on the conclusion of the part above, PRI was a suitable vegetation index for monitoring the severity of yellow rust disease in winter wheat. Therefore, in this study, PRI was used to establish the linkage between the disease severity and the hyperspectral data. Specifically, the yellow rust infection would be apparent at anthesis stage, and this should be closely related with the subsequent yield loss. Therefore, we chose the PHI image at this stage to form the SKB. To obtain a better fitting model, we reanalyzed the PHI-PRI and corresponding DI (%) data at the anthesis stage specifically, and obtained a linear regression model. It should be noted that the data range of DI must be between 0 and 100%. Any predicted DI results that were $>100\%$ or $<0\%$ were redefined as DI = 100% and DI = 0% to represent very infected plants and healthy plants, respectively.

2.3.1.6 Simulation of the wide band reflectance

The second step of constructing the SKB is to transform the hyperspectral reflectance of PHI-pixels to wide band reflectance of HJ-pixels. To achieve this goal, the best approach is the inherent relative spectral response (RSR) function of the HJ-CCD sensor. By integrating the hyperspectral reflectance of PHI-pixels on the RSR function, the band reflectance of HJ-CCD sensor was thus obtained. Besides, although the wavelength range of the fourth band of HJ-CCD sensor (760 nm-900 nm) was slightly exceeded the maximum wavelength of PHI sensor (850 nm), for most ground measured spectra, the reflectance basically kept on steady from 760 nm to 900 nm. Hence, the simulating results generated using the incomplete range of wavelength (760nm-850nm) should approach to the true value. The integration can be shown as follows:

$$R_{TM} = \int_{b_{start}}^{b_{end}} f(x)dx$$

where R_{TM} is the simulated reflectance of a certain band; b_{start} and b_{end} indicate the beginning and the end wavelength of this band respectively; $f(x)$ indicates the RSR function, which is obtained from CRESDA.

2.3.1.7 Spectral characteristics of different degrees of disease severity

Another way to define the disease severity of an undefined pixel, apart from the DI (%) value, is to quantify disease severity by severity classes. The criterion of severity class provided by Huang et al. (2007) was adopted, which corresponded to the major physiological alteration of diseased plants. The DI (%) thresholds for each severity class were: $DI<1\%$ indicated not infected (NI), $1\%<DI<10\%$ indicated a low degree of infection (LI), $10\%<DI<45\%$ indicated mid-range infection (MI), $45\%<DI<80\%$ indicated seriously infected (SI) and $DI\ (\%)>80\%$ indicated very seriously infected (VI). The MNF transformation and PPI function, which are used for noise reduction and end-member identification, were applied here to select the most representative pixels from the PHI image, and to form the typical spectrum for each severity class.

2.3.1.8 Spectral matching algorithms

The basic idea of spectral matching is to identify a set of pixels in the SKB that are the closest to the undefined pixel in terms of spectral characteristics. Before matching, each pixel should be standardized to eliminate systematic variation caused by aerosol conditions or other factors as follows:

$$R_{nor} = \frac{R - R_{\min}}{R_{\max} - R_{\min}}$$

where R_{nor} is the standardized reflectance of a certain band, R is the original reflectance, and R_{min} and R_{max} are the minimum and maximum band reflectance values, respectively, of the corresponding pixel.

Mahalanobis distances (Mah) and Spectral angle (SA) were selected as the distance measurement criterion. Both types of distance measurements had been proved to be with high efficiency in reflecting the spectral discrepancy (South et al., 2004; Goovaerts et al., 2005; Becker et al., 2007). The Mah distance can be written as:

$$D_M(x) = \sqrt{(x - x_R)\sum^{-1}(x - x_R)^T} \quad x=(x_1,x_2,x_3,x_4),\ x_R=(x_{R1},\ x_{R2},\ x_{R3},\ x_{R4})$$

where $x_{1\text{-}4}$ are the reflectance of the pixel under test in band1 to band4, respectively; $x_{R1\text{-}4}$ are the simulated reflectance of a specific pixel in SKB. $\sum$ is the covariance matrix between x and x_R.SA can be calculated by the following formula:

$$\theta = \arccos \frac{\sum_{i=1}^{4} x_i x_{Ri}}{\sqrt{\sum_{i=1}^{4} x_i^2}\sqrt{\sum_{i=1}^{4} x_{Ri}^2}} \quad \theta \in \left[0, \frac{\pi}{2}\right]$$

To determine the DI (%) or class of disease severity of an undefined pixel, we have to calculate the Mah and spectral angle from this pixel to each pixel or class in the SKB. A longer distance or larger angle indicates that the pixel deviated from the undefined pixel, whereas a shorter distance or smaller angle indicates that it is similar to the undefined pixel. By selecting the most similar pixel, the severity class of an undefined pixel can be determined. To determine the DI (%) of a certain pixel, the weighted average method was used. According to the distance criteria above, the five most similar pixels were selected from the SKB. For each band of these pixels (here we used the hyperspectral bands extracted from the PHI image), the reflectance was processed according to the following equation:

$$R_E = \frac{\sum_{i=1}^{k} R_i \times \frac{1}{d_i}}{\sum_{i=1}^{k} \frac{1}{d_i}}$$

where R_E is the estimated reflectance of a certain pixel through k-NN estimation; R_i is the reflectance of the i_{th} nearest pixel according to the ranking order of the distance; d_i is the distance between the pixel under test to the i_{th} nearest pixel.

2.3.1.9 Verification

To verify the performance of SKB in identifying and monitoring the severity of yellow rust diseases, two datasets were used: the simulated data and the field-measured data with corresponding satellite images.

1. Verification of SKB using simulated data
   The simulated data comprised 50 randomly selected pixels in the same experimental field, but outside the three regions selected for constructing the SKB. The hyperspectral information of each pixel was used to create the reference DI (%) and severity class with the empirical model and the corresponding threshold for each severity class. To test the performance of SKB in terms of DI (%) value, we estimated the DI value with both distance criteria described above. The samples were split into two: the pixels with a reference DI between 1 and 100%, i.e. the 'diseased' pixels, and those with a reference DI＜1%, i.e. 'healthy' pixels. For the diseased pixels, the estimated DIs were compared with the reference DI by Pearson correlation analysis and the normalized root mean square error (NRMSE). For the healthy pixels, we used 'yes or no' to determine whether the estimated value indicated infection or not, which also provided an accuracy ratio. The estimation of severity class was verified by overall accuracy and the kappa coefficient.
2. Verification of SKB using field surveyed data
   The field surveyed data sets included the ground investigation of disease severity and the corresponding HJ-CCD images. Between June 1–3, 2009, when the winter wheat was at the anthesis stage, we conducted a survey in the southeast of GanSu Province. The climate of the area surveyed is characterized by high humidity and rainfall, and yellow rust disease occurs almost every year. This area has similar environmental conditions and cultivation customs to those where we constructing the SKB in Beijing, and this makes it an appropriate place for model verification. With the aid of the local Department of Plant Protection, 26 plots were randomly selected and surveyed in the area (Fig. 9). To relate the surveyed value to the pixel value of the HJ-CCD image, we defined the plot as a uniformly planted winter wheat region with an area no less than 30 m in radius. The geographical coordinates of each plot were measured by GPS at the centre of the plot. Disease severity was measured as described above. We repeated the measurement in five evenly-distributed sections in each plot, and 20 individual plants were included in each measurement. The HJ-CCD images (ID: 122516, 122518) acquired on June 2, 2009 completely covered the surveyed area. The raw data from the HJ-CCD imagery was calibrated based on the corresponding coefficients provided by CRESDA. The calibrated data were atmospherically corrected with the algorithm provided by Liang et al. (2001), which estimated the spatial distribution of atmospheric aerosols and retrieved surface reflectance under general atmospheric and surface conditions. The images were also geometrically corrected against historical reference images with the same geographical coordinates. The images were rectified with a root mean square error of less than 0.5 pixels. The spectrum of the each plot was extracted from the image according to the GPS records. The estimated accuracy in this step followed the same process as the simulated data.

2.3.2 Results

There were 7918 pixels included in the process of constructing the SKB. The linear regression model between DI (%) and PRI at anthesis stage could be illustrated as follows:

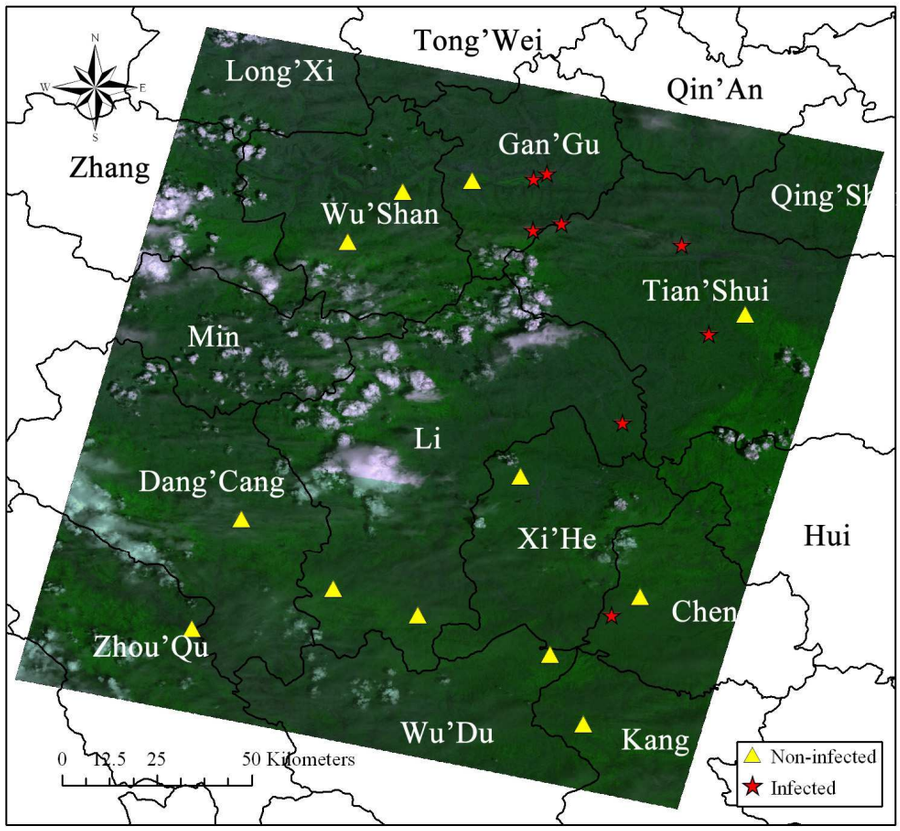

Fig. 9. The field surveyed area in Gansu Province. The base image is the HJ-CCD image acquired on June 2, 2009

$$DI(\%) = -538.98 \times PRI + 2.0983 \quad (R^2=0.88)$$

The pairs of DI (%) and PRI were plotted in Fig.4, which showed a significant correlation (R^2 = 0.88). Based on the model, there were 85 pixels with a DI of 100% and 3991 pixels with a DI between 1%and 100%, indicating 51.5%pixels infected to a varied degree of severity, whereas the other 48.5% pixels (DI = 0%) were healthy plants. In the experimental field, the variation in the degree of severity of yellow rust from totally healthy plants to very infected plants provided the essential diversity or heterogeneity of infection, which then enabled establishment of the SKB. The MNF transformation resulted in 9 leading eigenvectors with eigenvalues greater than 4.0 (Fig. 10), and these were used for further analysis.

2.3.2.1 Performance of SKB for simulated data

In the simulated dataset, there were six healthy pixels and 44 diseases affected ones. When estimating DI (%), one pixel with no infection was estimated as infected by the Mah distance criterion, whereas with the SA criterion two were mislabeled. Fig.11 shows the scatter of the disease affected pixels plotted in relation to reference DI and estimated DI; the average reference DI is 36%. The reference DIs and estimated DIs were strongly and linearly correlated for both the Mah distance (R^2 = 0.90) and SA (R^2 = 0.84) criteria. Further, the NRMSE of Mah distance and SA were 0.20 and 0.24, respectively, indicating that the SKB can estimate DIs accurately from the simulated multi-band reflectance.

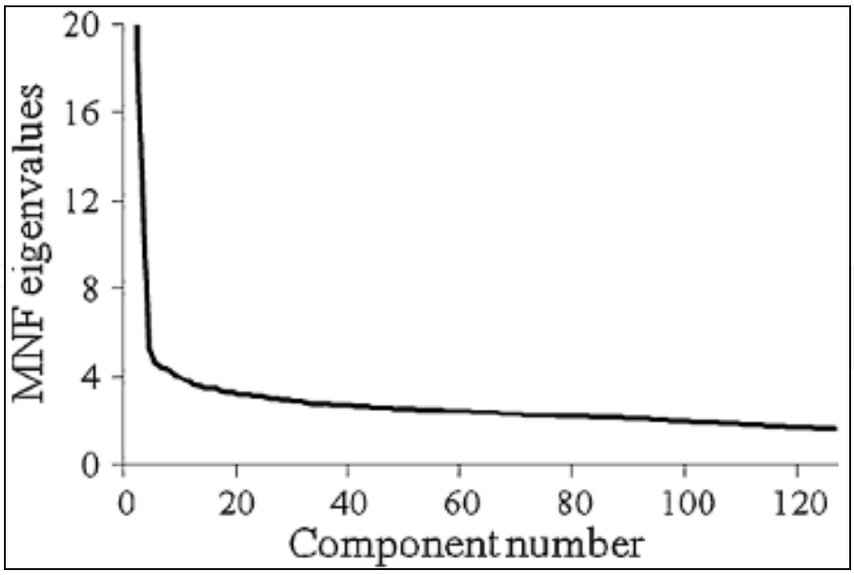

Fig. 10. MNF eigenvalues variation trend

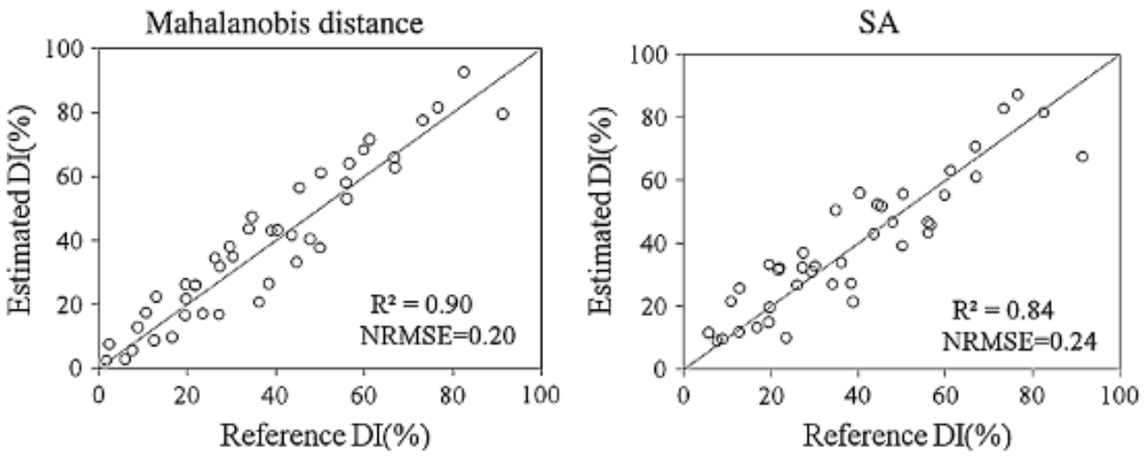

Fig. 11. Estimated DI(%) using simulated data

Table 6 gives the reference class of disease severity and the estimated class in the form of an error matrix. The overall accuracy with Mah distance and the SA criterion were 0.80 and 0.76, respectively, whereas the kappa coefficients were 0.71 and 0.65, respectively. However, we noticed that all the misclassified pixels were assigned to no more than one class adjacent to the reference class. Therefore, for simulated data, the classification accuracy was satisfactory in determining the severity class of yellow rust by SKB.

2.3.2.2 Performance of SKB for field surveyed data

Apart from the verification against simulated data, more importantly, the field surveyed data can be also used to assess the performance of the SKB. The field investigation showed that eight out of 26 plots were infected with DI ranged from 4 to 90%, whereas the other 18 plots were not affected by yellow rust. The estimation by DI (%) successfully identified the eight infected plots when the Mah distance criterion was used, whereas the SA criterion

		Reference					
		None	Low range	Mid range	Serious	Very serious	Total
Estimation (Mah)	None	6	0	0	0	0	6
	Low range	0	5	2	0	0	7
	Mid range	0	1	20	2	0	23
	Serious	0	0	1	10	1	12
	Very serious	0	0	0	1	1	2
	Total	6	6	23	13	2	50
Estimation (SA)	None	5	1	0	0	0	6
	Low range	1	4	1	0	0	6
	Mid range	0	1	20	2	0	23
	Serious	0	0	2	9	1	12
	Very serious	0	0	0	2	1	3
	Total	6	6	23	13	2	50

Table 6. Error matrix for simulated data

resulted in one misestimated plot. Figure 7 shows the scatter of the eight data plotted in relation to reference DI and estimated DI for both distance criteria. There was a significant linear trend in graphs based on both the Mah distance and SA criteria. The R^2 of Mah distance and SA were 0.80 and 0.67, respectively, whereas the NRMSE were as high as 0.46 and 0.55. In real circumstances, approximately 50% error in the estimated disease index is unsatisfactory. On the other hand, however, most of the uninfected plots were correctly identified according to DI (%) estimates (i.e. a DI<1%). For both the Mah distance and SA criteria, 15 out of 18 non-infected plots had been identified correctly, resulting in an accuracy of 77.8%. The results for estimating disease severity by severity class were even more encouraging. The overall accuracy for the Mah distance and SA criteria were 0.77 and 0.73, respectively, whereas the kappa coefficients are 0.58 and 0.49, respectively. Table 3 gives the error matrix for both criteria. The misclassified pixels were also assigned exclusively to the adjacent class.

In general, the above results demonstrate that the proposed SKB scheme has great potential for detecting the incidence and severity of yellow rust through multispectral images. As shown from several previous studies, the image processing method of MNF transformation was efficient in extracting the principle information from the images related to wheat disease infection (Zhang et al. 2003; Franke and Menz 2007). For the present study, we found that coupling MNF transformation with the PPI function was an appropriate way of extracting the principle information on yellow rust disease. To estimate disease severity by DI (%), the proposed SKB has achieved a satisfactory accuracy for simulated data. However, the estimated accuracy for field surveyed data was unsatisfactory, implying that the method tends to underestimate or overestimate the disease severity in practice. Nevertheless, to estimate disease severity through disease severity class has achieved a satisfactory accuracy for both simulated data and field surveyed data. Therefore, the disease severity class seems to be more robust in

determining the disease severity. This might be because it is more rough estimation than DI (%). It is understandable that for the same sample, the less precise the criterion, the greater accuracy it would achieve. Moreover, the 5-class disease severity quantification is enough to guide field applications. We suggest that DI (%) should be used for detecting the disease severity of yellow rust by SKB. For the distance criteria used in the process of matching with SKB, the Mah distance criterion might be more appropriate because it performed better than SA in all the analyses conducted in this study (Figs. 11, 12, Tables 6, 7). Some previous studies have already emphasized the potential of hyperspectral imagery (Bravo et al. 2003; Moshou et al. 2004; Huang et al. 2007) and the high-resolution of multispectral imagery (Franke and Menz 2007) for detecting yellow rust disease. The development of SKB in the present study can be viewed as a scaling up method, which has extended the capability of detecting yellow rust disease from hyper- spectral imagery to the moderate resolution of multispectral imagery. However, it should be noted that the task of monitoring the occurrence and degrees of infection of crop diseases is far more complex than the cases described in this study. The spectral characteristics of yellow rust infection might appear similar to other sources of stress. In addition, the impact of phenology, cultivation methods, fragmentation of farmlands and other environmental conditions would also increase the difficulty and uncertainty of the estimation process. Therefore, the SKB developed in this study should correspond to the situation at the anthesis stage exclusively, and is only suitable for those regions with similar environmental characteristics and cultivation methods. For other regions with significantly different environmental characteristics, this purposed SKB may not work well. The possible solution to these problems may include incorporating suitable priors, which would require integration strategies and understanding of the mechanisms underlying some fundamental processes. Further research is required to address the problems mentioned above.

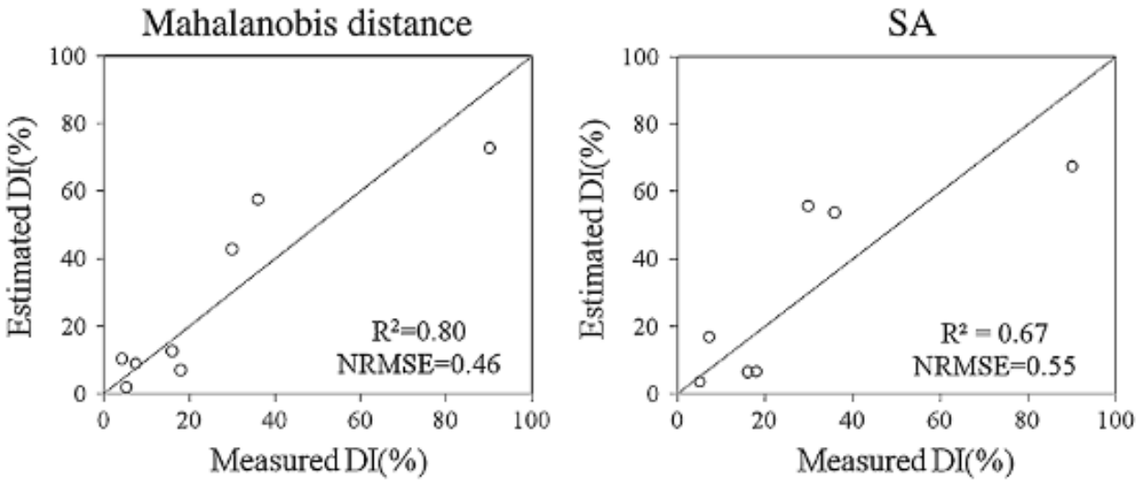

Fig. 12. Estimated DI(%) using field measurements

2.3.3 Conclusion

The low spatial resolution and few spectral bands have limited the application of moderate resolution satellite images for monitoring yellow rust disease. The spectral knowledge base developed enabled disease incidence and severity to be detected by moderate resolution satellite images. The SKB supported two ways of estimating disease severity: the disease

		Reference					
		None	Low range	Mid range	Serious	Very serious	Total
Estimation (Mah)	None	16	0	0	0	0	16
	Low range	2	2	1	0	0	5
	Mid range	0	1	3	0	0	4
	Serious	0	0	0	0	1	1
	Very serious	0	0	0	0	0	0
	Total	18	3	4	0	1	26
Estimation (SA)	None	15	0	0	0	0	15
	Low range	3	2	1	0	0	6
	Mid range	0	1	3	0	0	4
	Serious	0	0	0	0	1	1
	Very serious	0	0	0	0	0	0
	Total	18	3	4	0	1	26

Table 7. Error matrix for ground measured data

index and disease severity class. Both methods of estimation achieved a satisfactory level of accuracy for simulated data. For field surveyed data, estimation by DI (%) resulted in an unsatisfactory level of accuracy, whereas it was satisfactory for severity class. The Mah criterion performed better than spectral angle in all analyses. Therefore, the former should be considered as the more appropriate distance criterion.

Generally, the purposed SKB has a great potential in extending the capability of detecting yellow rust to multispectral remote sensing data, especially when the region of interest has similar environmental conditions to where the SKB was developed. The uncertainties caused by environmental differences should be further investigated in future studies.

2.4 Detecting yellow rust of winter wheat using land surface temperature (LST)

The air temperature and humidity are the most direct and important indicators of occurrence of yellow rust fungal. Generally, weather stations can provide the dynamic pattern of meteorological data for site sampled, yet not able to include the information of spatial heterogeneity. Fortunately, remote sensing technology has great potential for providing spatially continuous observations of some variables over large areas (Luo et al., 2010). The aim of the study was to study preliminarily on the relationship between the occurrence of wheat yellow rust and land surface temperature (LST) derived from moderate-resolution imaging spectroradiometer (MODIS) in order to predict and monitor incidence of the yellow rust on large scale.

2.4.1 Materials and methods

2.4.1.1 Survey area and field investigations acquisition

Field experiments of winter wheat were conducted during the growing seasons (form April to June) of winter wheat in 2008 and 2009. The investigation locations included Longnan

district, Tianshui district, Dingxi district and Pingliang district in GanSu province and Qingyang district in ShanXi province as well as Linxia district in Ningxia Hui Autonomous Region (Fig.1), where the climates are semiarid and subhumid. Survey areas are located between latitude 32º40′N to 35º39′N and longitude 103º10′E to 107º40′E, and the mean altitude is over 2000 meter. The climate condition of surveyed area is characterized by high humidity and rainfall, and yellow rust disease almost occurs every year. It is reported that Longnan district is an important overwintering and oversummering area of yellow rust fungal (Zeng, 2003).

With the aid of the local Department of Plant Protection, 151 plots, including 68 plots from April to June in 2008, and 83 plots from April to June in 2009, were randomly selected and surveyed in the areas. The geographical coordinates of each plot were measured by GPS navigator at the middlemost of the plot. In addition, the disease severity was inspected.

2.4.1.2 MODIS land surface temperature (LST) products (MOD11)

Product description

MODIS Land Surface Temperature and Emissivity (LST/E) products (named starting with MOD11) provide per-pixel temperature and emissivity values. Temperatures are extracted in Kelvin with a view-angle dependent algorithm applied to direct observations. This method yields the error less than 1 K for materials with known emissivity. The view angle information is included in each LST/E product.

MOD11 acquisition and processing

24 MOD11A2 images（MODIS/Terra land surface temperature/emissivity 8-day L3 global 1km SIN grid v005）were acquired for free from Web (http://edc.usgs.gov/#/Find_Data) from April to July in 2008 and 2009, which covered completely the survey area, and 4 scenes images were acquired in every month. The raw data of MOD11A2 imagery were processed and transformed by MRT tool, and LST products were extracted from MODII A2 images. Then the survey area was cut by ENVI from LST images. Followed by that step, 4 scenes 8-day LST images of every month were all averaged, and 6 average LST images, including April, May, June in 2008 and 2009, were obtained. Finally, LST of 151 investigation points were respectively extracted from 6 average LST images.

2.4.2 Result

2.4.2.1 Determining LST threshold of infected points

The spatial resolution of MODIS temperature products is 1 km, while the DI of every investigation point only stands for the incidence of 30 m in semi diameter plots. Therefore, the scale of MODIS temperature products seemed not satisfied the investigation points for proper relationship between them. However, spatial variability of LST is slim, and the law still exists. A series of results could be found by establishing a two-dimensional spatial coordinate based on DI and LST, in which all investigation points were displayed (Fig 13). Firstly, the DI ranged from 0% to 100%, and most of infected points ranged from 0% to 60%. The LST values were between 292K and 310K with most of infected points distributed in the range from 298K to 306K. In addition, the points in the region of less than 298K were not infected by yellow rust basically; DI were less than 1% expect for one point (296.29K, 16%),

which was thought as abnormal point. In addition, the LST values of all investigation points were less than 306K expect for one point (310.09K, 24%), which was abnormal because its LST was far away from LST values of others.

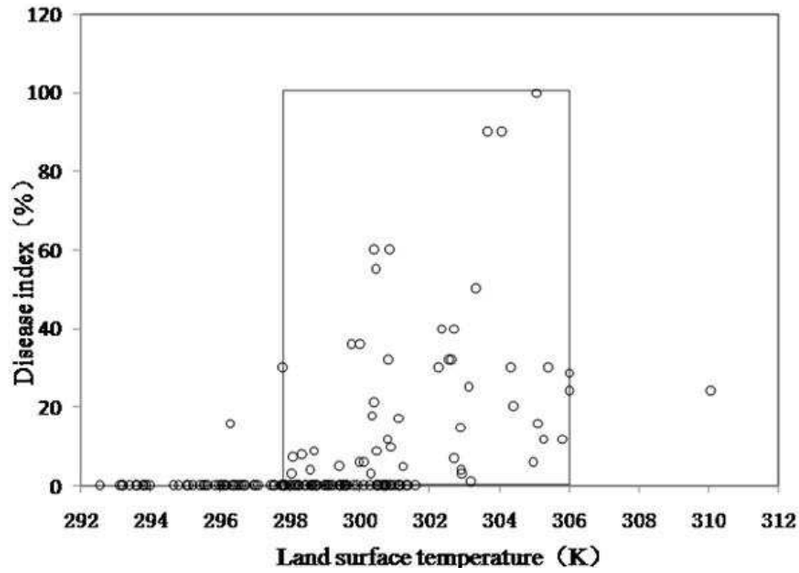

Fig. 13. The distribution of the investigation points

Therefore, without considering other factors, It is concluded that yellow rust can occur when LST is in the region from 298K to 306K.

2.4.2.2 Yellow rust incidence analysis based on LST

According to the results illustrated above, the advanced analysis was performed for incidence and possible area of yellow rust. The points in different LST range were done statistical analysis with all points' numbers and the infected points' number, and finally, the incidences were obtained by the number of the infected points dividing the number of all points in the different LST range (Table.8). The result showed that all investigation points in the region of less than 298K were not infected by yellow rust, except for the abnormal point (296.29K, 16%). On the other hand, in the LST region of more than 306K, there was only one point, which was viewed as abnormal point (310.085K, 24%). Thereby, it is quite possible that yellow rust fungus can not survive in the region of more than 306K. The conclusion was consistent with the above result (Fig. 13).

LST (K)	LST≥296	LST≥297	LST≥298	LST≥299	LST≥300	LST≥301	LST≥302	LST≥303	LST≥304	LST≥305	LST≥306
Total number	126	112	99	79	61	34	25	16	12	8	1
Number of infected points	49	48	47	42	39	27	25	16	12	8	1
Incidence (%)	38.89	42.86	47.47	53.16	63.93	79.41	100	100	100	100	100

Table 8. Statistic analysis in different LST range

Furthermore, there was an increasing trend of incidences with the rising of LST in the region from 296K to 302K. The incidence of yellow rust reached up to 100% when the LST was graeter than 302K (Fig. 14).

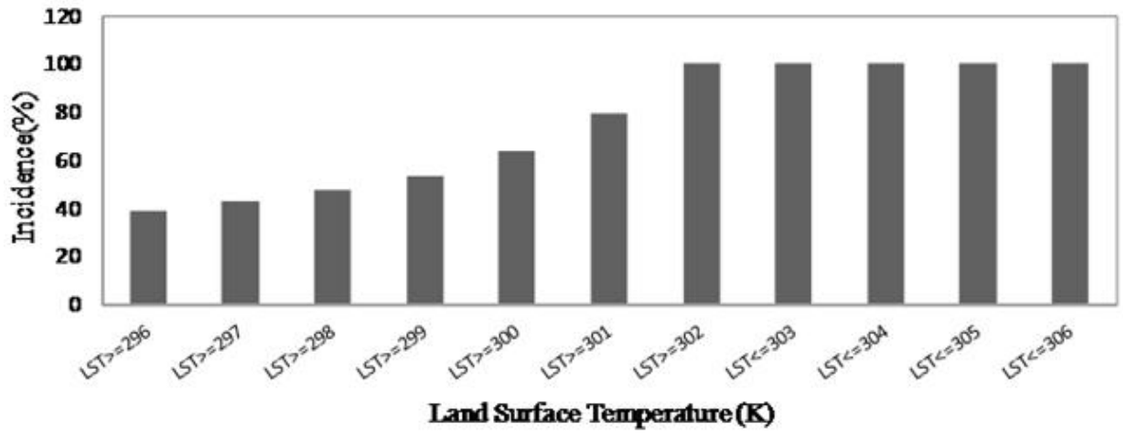

Fig. 14. The incidence of yellow rust in different LST range

2.4.2.3 Dividing yellow rust suitable occurrence region based on LST

According to Table 8 and Fig. 14, the survey areas could be divided into yellow rust unsuitable area (NSA), of which LST ranged from 298K to 306K, and yellow rust suitable area (SA), of which the LST was less than 298K and more than 306K. Moreover, the SA was divided into 3 levels according to the infected of yellow rust incidence and LST, and the LST thresholds for each level were: 298K ≤ LST ≤ 299K the low suitable area (LSA), on which the yellow rust occurs with very low possibility (incidence < 60%), 299K ≤ LST ≤ 301K the medium suitable area (MSA), which had moderate possibility for the occurrence of yellow rust (60% <incidence < 100%), and 302K ≤ LST ≤ 306K high suitable area (HSA), of which the environment was highly favorable to yellow rust (incidence=100%).

2.4.2.4 Verification

Total 26 points (from May 2008) were applied for the verification the method of estimating the incidence of yellow rust. It should be noted that those points were not used for the defining of the LST thresholds. (Fig. 15). These 26 points were constituted by 18 infected points and 8 non-infected points. Results showed the infected points were all in different suitable areas of wheat yellow rust, while the non-infected points were all in the unsuitable area. Thus the infected situation of yellow rust of these 26 points was consistent with forecast results. Geographically, it seemed that the yellow rust was prone to be prevalent in the northeast of Pingliang, southwest of Qingyang, northeast of Dingxi, the center part of Tianshui, and the west of Longnan, because they all were located in MSA and HAS. This result was consistent with the previous study (Xiao, et al, 2007). To prevent yellow rust from prevalence, more efforts should be placed on the farmlands located in the MSA, HAS and LSA.

2.4.3 Conclusions

Plant disease is governed by a number of factors, and the habitat factors play a major role in the development and propagation of fungal pathogens (Sutton et al., 1984; Hélène et al.,

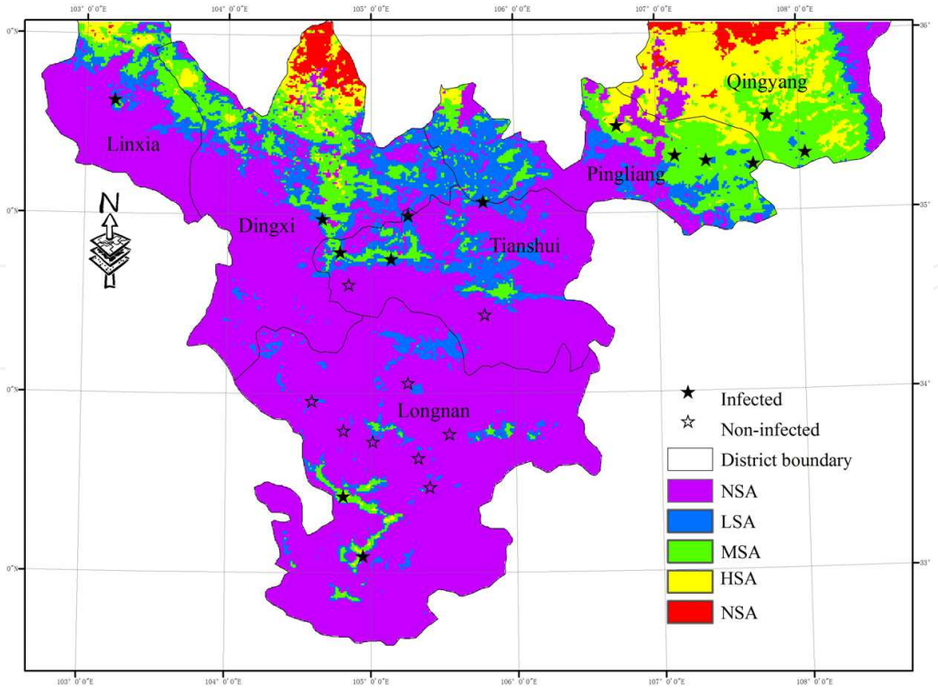

Fig. 15. Forecast map of yellow rust and distribution of measured points in May, 2008 based on LST

2002; Cooke et al., 2006). The yellow rust is no exception. The weather station can only offer points data, and remote sensing, however, can be a promising means for acquiring spatially continuous observations over large area. It has not been reported, if any, that the LST derived from remote sensing data is used to forecast the development of yellow rust.

The study tried to present a method that could forecast the suitable areas of wheat yellow rust by MODIS temperature products in a large scale. And it was proved that LST derived from remote sensing data had potential for predicting the occurrence and development of wheat yellow rust in a large area. From our results, it is clear that preventive measures of yellow rust can been made over large scale area accordingly with different real-time prediction methods based on LST derived from remote sensing data.

3. Detecting and discriminating winter wheat aphid by remote sensing

Wheat aphid, Sitobion avenae *(Fabricius)*, is one of the most destructive pests in agricultural systems, especially in temperate climates of the northern and southern hemispheres. Wheat aphid appears annually in the wheat planting area of China, causing great economic damage to plant crops as a result of their direct feeding activities. In high enough densities, wheat aphids can remove plant nutrients, and potentially reduce the number of heads, the number of grains per head, and overall seed weight. The damage is especially high when wheat aphid occurs in the flowering and filling stage of wheat. It is reported that average densities over 20 aphids per plant can cause substantial losses of yield and quality of wheat (Basky & Fónagy, 2003). There are also indirect damages including excretion of honeydew from aphids and as a vector of viruses, most notably two strains of the Luteovirus Barley Yellow Dwarf Virus (BYDV-MAV and BYDV-PAV) (Susan et al, 1992). To prevent the

occurrence and prevalence of aphid, large amounts of insecticides are used, causing environment pollution. Therefore, large-scale, real-time prediction and monitoring of wheat aphid incidence and damage degree using remote sensing technology are extremely important.

3.1 Detecting winter wheat aphid using hyperspectral data

The study aimed to identify spectral characteristics of wheat leaf and canopy infected by aphid and find the sensitive bands to aphid at canopy level in filling stage of wheat, and to establish an aphid damage hyperspectral index (ADHI) based on those sensitive bands for detecting aphid damage levels in wheat canopy level in filling stage of wheat.

3.1.1 Materials and methods

3.1.1.1 Field experiments and field inventory

The field experiment plot was located at Xiaotangshan Precision Agriculture Experiment Base, Changping distract, Beijing (40°10.6'N, 116°26.3'E). The experimental field was about 250 m in length and 80 m in width. The winter wheat was planted in the study area from Oct 3, 2009, and harvested from June 25, 2010. Field inventory was conducted on June 7, 2010 when wheat was in the filling stage. Twenty five ground investigations including different aphid damage levels were selected. Aphid damage level was surveyed according to the investigation rule.

3.1.1.2 Canopy spectral measurements

Please refer to 1.1.1.2 part above.

3.1.2 Results

3.1.2.1 Leaf spectral characteristics of wheat infested by aphid

Representative reflectance measured from wheat aphid-infested and uninfested wheat leaves are shown in Fig. 16. It was evident that the spectral response of the wheat leaf was significantly affected by wheat aphid feeding (Fig. 16). The reflectance of wheat leaf infested by aphid was higher in the visible spectrum and short-wave infrared region and lower in near-infrared region than that of uninfested leaf. A significant increase in the reflectance from the wheat aphid-infested leaf in the visible region (400-700 nm) was observed, evidently due to reduction of photosynthetic pigment concentrations in particular chlorophylls caused by wheat aphid feeding (Richardson et al., 2004).

3.1.2.2 Canopy spectral characteristics of wheat infested by aphid

Compared with the canopy spectra of the healthy wheat, the canopy reflectance of aphid-infested wheat was gradually decreased in the range from 350 nm to 1750 nm, especially in the near infrared region (Fig. 17). Previous researches indicated that wheat had higher reflectance at visible wavelengths than the healthy vigorously growing wheat because the photoactive pigments (chlorophylls, anthocyanins, carotenoids) were destroyed. In this study, aphid occurred in the filling stage of wheat and the honeydew excreted by aphid absorbed dust or others from surrounding environment and contaminated (darkened) the leaf surface. As a result, the absorption at light slight wavelengths became stronger instead of weaker.

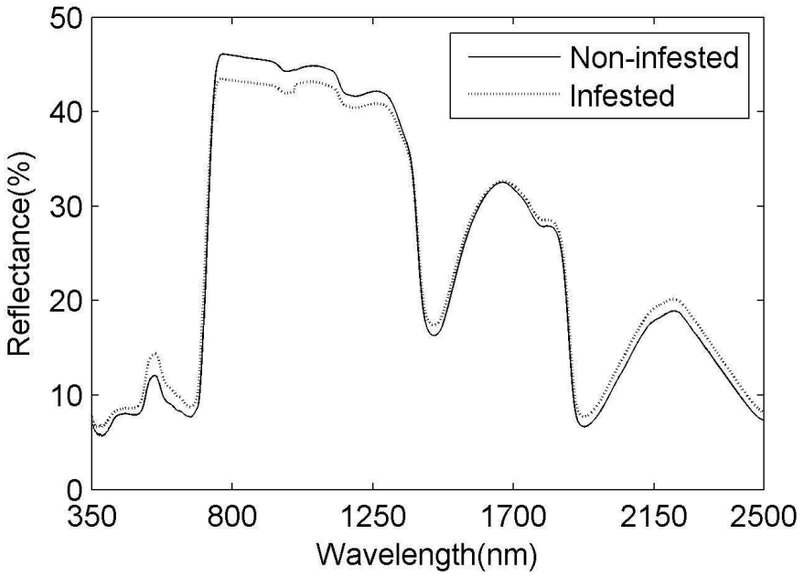

Fig. 16. The spectral reflectance of winter wheat leaf uninfested and infested by aphid

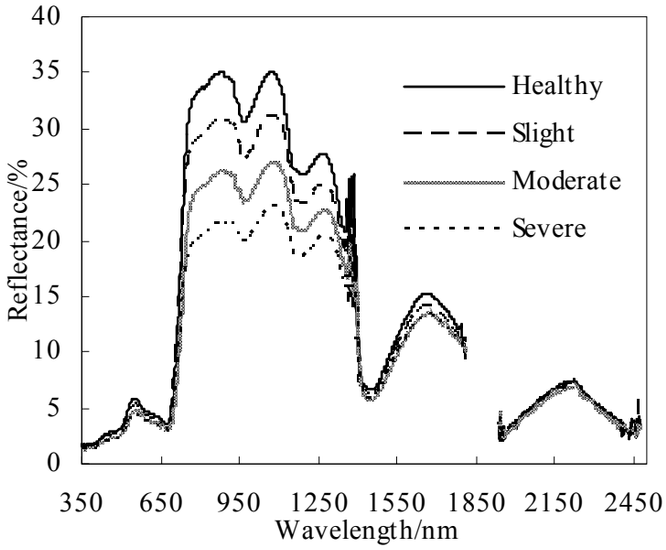

Fig. 17. The spectral reflectance of healthy wheat and wheat infested by various aphid damage levels. (Healthy: the average spectra of healthy wheat samples; Slight: the average spectra of aphid damage level 1and 2; Moderate: he average spectra of aphid damage level 3and 4; Severe: the average spectra of aphid damage level 5 and 6).

3.1.2.3 Aphid damage hyperspectral index for detecting aphid damage degree

Sensitive band selection of aphid infestation based on canopy reflectance

The sensitive bands were selected out by relevance analysis between reflectance and aphid damage levels. The reflectance ranges were from 400 nm to 690 nm, from 700 to 1300 nm and from 1500 to 1800 nm. The most sensitive bands to aphid were 551 nm (R^2=0.741) in

visible light, 823 nm (R^2=0.865) in near infrared (NIR) and 1654 nm in short-wave infrared (SWIR) (R^2=0.668), respectively (Fig. 18).

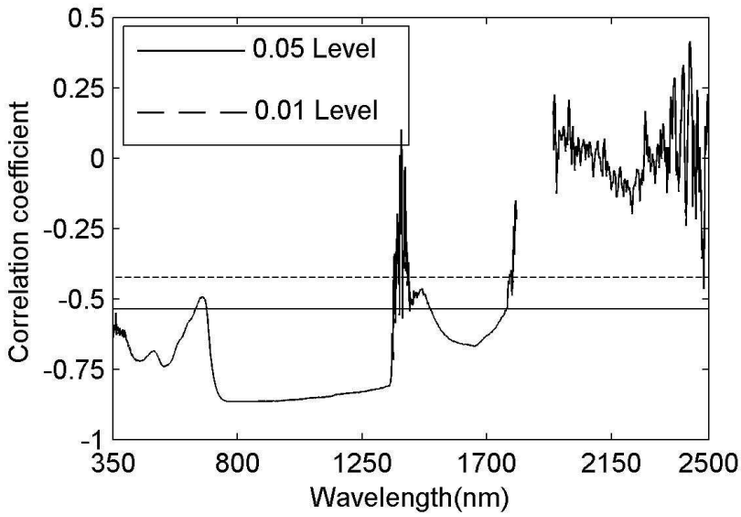

Fig. 18. Correlation coefficient between reflectance and aphid damage levels

Aphid damage hyperspectral index (ADHI) was established based on the most sensitive bands from hyperspectral data in the visible light region, NIR and SWIR and weight coefficient calculated according to rate of change of reflectance between healthy wheat and aphid-infected wheat, respectively.

$$\text{ADHI} = 0.32 \times \frac{\text{R551}_{normal} - \text{R551}_{infested}}{\text{R551}_{normal}} + 0.51 \times \frac{\text{R823}_{normal} - \text{R823}_{infested}}{\text{R823}_{normal}} + 0.17 \times \frac{\text{R1654}_{normal} - \text{R1654}_{infested}}{\text{R1654}_{normal}}$$

where $R551_{normal}$，$R823_{normal}$ and $R1654_{normal}$ are reflectance in 551 nm, 823 nm and 1654 nm of healthy wheat; $R551_{infested}$, $R823_{infested}$, $R1654_{infested}$ are reflectance in 551 nm, 823 nm and 1654 nm of aphid-infected wheat; 0.32, 0.51 and 0.17 are weight coefficients calculated by the contribution to change rates.

Further more, the correlation analysis was conducted between ADHI and aphid damage level from 25 investigation points (Fig. 19). It was concluded that ADHI exhibited high relationship with aphid damage levels (R^2=0.839). Therefore, ADHI was an important index to estimate aphid damage level in winter wheat.

3.1.3 Conclusions

Hyperspectral remote sensing has gone through rapid development over the past two decades and there is a trend toward the use of hyperspectral image in the application of remote sensing for precision farming. The study analyzed the spectral characteristics of wheat infested by aphid and selected the sensitive bands to aphid damage level. Then, an ADHI was developed using the most sensitive bands in visible light region, NIR and SWIR.

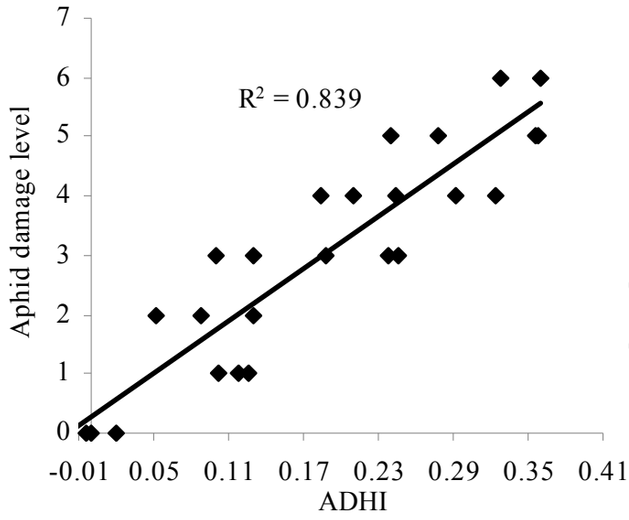

Fig. 19. The correlation between ADHI and aphid damage level

It was concluded that ADHI was a sensitive index to aphid damage levels, and could be used to retrieve aphid damage levels in the filling stage of wheat.

Crop growth is very dynamic processes and monitoring the condition of agricultural corps is a complex issue. It is possible that wheat damage symptoms caused by aphids and its response of canopy reflectance are different in different wheat growth stages. This study revealed that the reflectance of wheat infested by aphid was lower than healthy wheat in filling stage probably because of honeydew excreted by aphid. This was not consistent with previously published results in early detection of aphid infestation. Therefore, whether the ADHI can effectively retrieve aphid damage levels in other wheat growth stages remains as a task of future studies.

3.2 Detecting winter wheat aphid incidence using Landsat 5 TM

Wheat aphid occurrence and damage degrees are related to many factors including temperature, humidity, precipitation, field management, enemies, etc.. Most of the present studies on aphid prediction have been conducted based on meteorological data acquired from weather stations, and aphid density was monitored using the spectral characteristics of wheat infested by aphid. However, it is rare to investigate the relationship between environmental parameters, vegetable information derived from satellite images and aphid damage degrees. The aim of the present study is to investigate the relationships of aphid occurrence and damage degree to LST, NDWI, and MNDWI, which are related to vegetation water content derived from multi-temporal Landsat 5 TM. Another goal of the current research is to distinguish the degrees of aphid damage using 2-dimension feature spaces established by LST-NDWI and LST-MNDWI.

3.2.1 Materials and methods

3.2.1.1 Study areas

The study areas are selected in Shunyi district (116°28'—116°58' E，40°00'—40°18' N) and Tongzhou district (116° 32'—116°56' E, 39°36' —40°02' N,) of Beijing, China (Fig.20-a). The

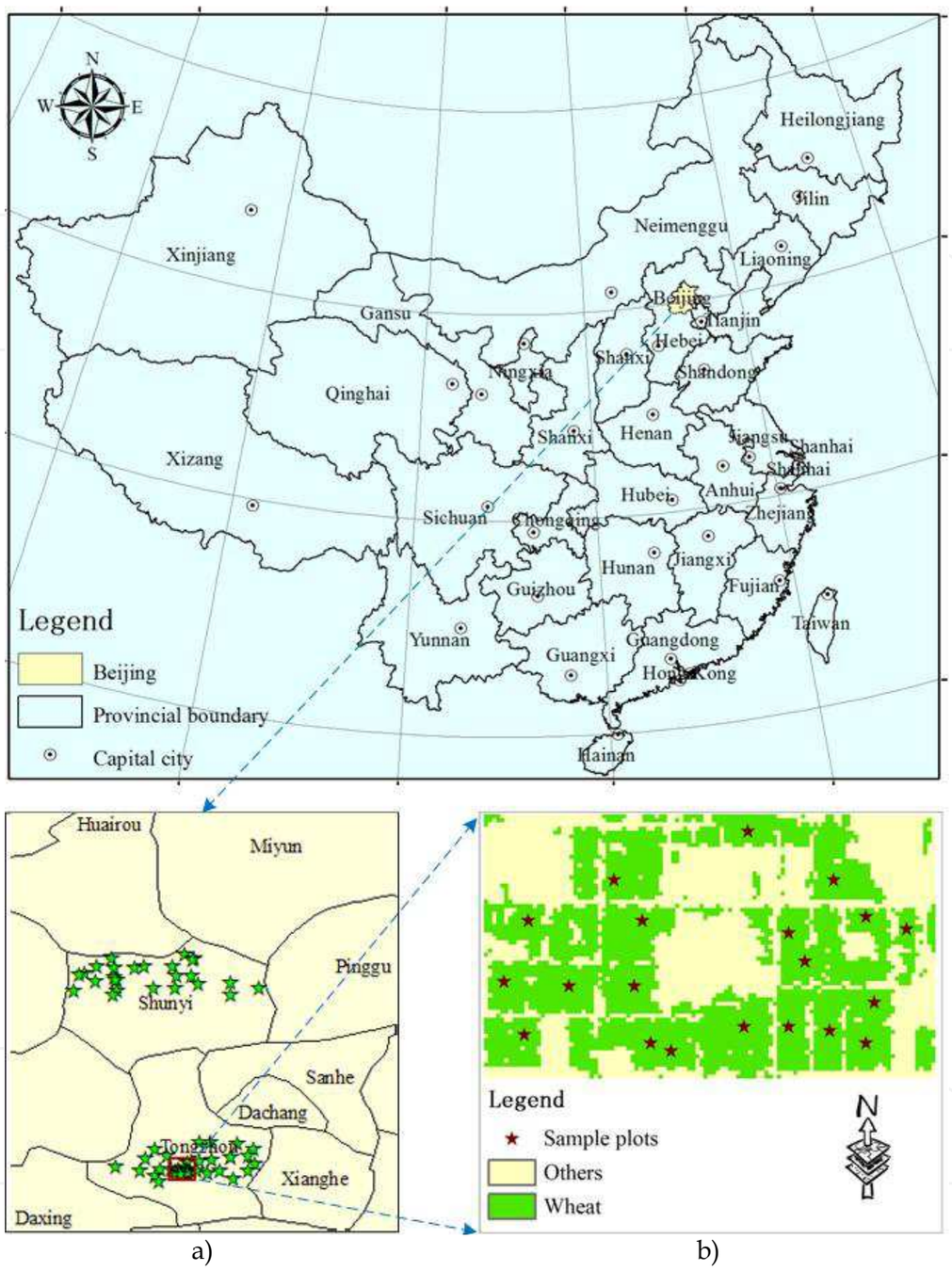

Fig. 20. The study area and the spatial distribution of sample plots

study areas have flat topography, with elevation ranging from 20 m to 40 m. The study areas have semi-humid warm temperate climate with yearly precipitation of 625 mm and mean temperature of 11.5°C in the Shunyi district and yearly precipitation 620 mm and mean temperature of 11.3°C in the Tongzhou district. Both districts are considered main winter wheat planting areas in Beijing, and aphid infestations occur in both areas almost every year.

3.2.1.2 Field inventory and data pre-processing

Field inventory was conducted during the growing seasons of winter wheat in 2010. The winter wheat in the study areas were planted between September 25 and October 7, 2009, and harvested between June 19 and June 25, 2010. Based on the combination of representative sampling and random sampling scheme, 70 sample plots with size of 0.09 ha (30 m × 30 m) each were collected as in Fig 1-a. These sample plots had different site conditions, plant densities, and management conditions. Aphid density surveys were carried out respectively on May 4 and May 6 for jointing stage, May 20 and May 21 for the heading stage, and June 3 and June 4 for the filling stage. The geographical coordinates of each plot were measured by global positioning system (GPS) (GeoExplorer 3000 GPS, with the error within 1m) at the middlemost of the plot.

Each sample covered with an area of 1 m^2. Then, 10 tillers in each sample plot were randomly selected, and the number of aphids was counted. The aphid densities were then estimated as follows: total aphids /10 tillers.

The survey results were divided into three aphid damage degrees according to the aphid density investigated for facilitating the study. They were S0: non-infested by aphid and no damage to wheat, S1: aphid abundance/per tiller was about 3-10 and damage degree to wheat was slight, and S3: aphid abundance/per tiller was more than 20 and damage degree to wheat was severe.

3.2.1.3 Satellite image acquisition and pre-processing

Three Landsat-5 Thematic Mapper (TM) images (path 123/row 32) and three MOD 02 1 KM-Level 1B Calibrated Radiances Production (MOD 02) were acquired on May 4, May 20 and June 5, 2010, respectively. And all images were more than 90% cloud-free.

The Landsat-5 TM images were spectrally corrected to reflectance using the Landsat TM calibration tool and FLAASH (Fast line-of-sight Atmospherics Analysis of Spectral Hypercubes) was used to correct the image for atmospheric effects in ENVI 4.5. The Landsat-5 TM images were geometrically corrected versus a reference IKONOS image (equivalent scale map 1:10000) of the same area, available from a previous study. The resulting root mean square error (RMSE) did not exceed 0.3 pixels, which was adequate for the purposes of the present study.

3.2.1.4 Derivation of LST, NDWI and MNDWI from Landsat 5 TM

NDWI and MNDWI are both sensitive to changes in liquid water content of vegetation canopies (Hunt and Rock, 1989). In the current research, both NDWI and MNDWI were used to determine the threshold of aphid occurrence and the aphid damage degree. The indices are of the general form, as shown in the following:

$$NDWI = \frac{R_{NIR} - R_{SWIR}}{R_{NIR} + R_{SWIR}} \quad MNDWI = \frac{R_{GREEN} - R_{SWIR}}{R_{GREEN} + R_{SWIR}}$$

where R_{GREEN} ,R_{NIR} and R_{SWIR} are the reflectance in the green band, near-infrared band and short wave infrared band, respectively. For Landsat TM/ETM+, R_{GREEN} ,R_{NIR} and R_{SWIR} correspond to band2, band4 and band5, respectively.

LST is the radioactive skin temperature of the land surface, which plays an important role in farm and ecological environment. The present paper aims to discuss the relationship between LST and aphid occurrence and spread. LST was derived from the thermal infrared band (10.4-12.5μm) data of Landsat-5 TM using generalized single-channel algorithm developed by Jiménez-Muñoz and Sobrino (Jiménez-Muñoz and Sobrino, 2004). Surface emissivity (ε) and atmospheric water vapor content (w) were important parameters in the generalized single-channel algorithm. In the study, w was derived from the reflectance of band2 and band19 of MOD02, (Kaufman and Gao, 1992), and ε was calculated by vegetation coverage (Carlson and Ripley, 1997).

The NDWI, MNDWI and LST of all sample points were calculated and extracted from the Landsat images.

3.2.1.5 Subset image selection and wheat extraction

We resized the subset areas with size of 7.2 km² (3 km × 2.4 km) from the study area image located in Tongzhou district and covered with 20 evenly distributed sample points, and the aphid densities of the sample points were surveyed on May 6, May 20 and June 4, 2010, respectively. The survey results showed that the aphid damage degree of all sample points were S0 on May 6, 18 points for S1 and 2 points for S0 on May 20, and 16 points for S2 and 4 points for S0 on June 4, respectively. The subset areas were small enough and 20 sample points evenly distributed, According to the survey result, the aphid damage degree of the sample plots was basically same. Thus, the change of the aphid damage degree of wheat pixels in the wheat plots was slim or even basically the same as the sample plots. The wheat area of subset image selection area was extracted using classification of decision tree in ENVI 4.5 (Fig 20-b). The LST, NDWI and MNDWI of 2000 wheat pixels were extracted.

3.2.1.6 Methods of accuracy assessment

One basic accuracy assessment currently being used is overall accuracy, which is calculated by dividing the correctly classified pixels by the total number of the pixels checked. The Kappa coefficient is a measure of the overall agreement of a matrix introduced to the remote sensing community in early 1983. It has since become a widely used measure for classification accuracy. In contrast to overall accuracy, the Kappa coefficient takes non-diagonal elements into account (Rosenfield and Fitzpatrick-Lins, 1986), and it is calculated by the formula:

$$K = \frac{N\sum_{i=1}^{r} X_{ii} - \sum_{i=1}^{r} X_i + X_{+i}}{N^2 - \sum_{i=1}^{r} X_i + X_{+i}}$$

where r is the number of rows and columns in the error matrix; N is the total number of observations; Xii is the observation in row i and column i; Xi+ is the marginal total of row I; X+i is the marginal total of column i.

3.2.2 Results

3.2.2.1 2-dimensional feature space based on LST-VI

The minimum value, maximum value, mean values and standard deviations of LST, NDWI and MNDWI with aphid damage degrees of wheat pixels in subset image selection were

listed in Table 9 and Table 10. And 2-dimensional feature space coordinates were established with LST as the abscissa and NDWI and MNDWI as the vertical axis, respectively (Figs. 2, 3). LST ranged from 287.5879 to 313.3448, NDWI ranged from 0.0226 to 0.5591 and MNDWI ranged from -0.3402 to -0.1077, respectively.

It is clear that LST was increasing from S0 to S1 to S2. LST was an important driving factor for aphid occurrence and could distinguish wheat non-infected from infested by aphids (Fig. 21 and Table 9). The general trend of NDWI increased firstly and reduced afterward, whereas MNDWI reduced firstly and increased afterward from S0 to S1 to S2.

Aphid Damage Degree	LST		NDWI		MNDWI	
	Minimum value	Maximum value	Minimum value	Maximum value	Minimum value	Maximum value
S0	287.5879	296.2498	0.0226	0.4405	-0.3402	-0.1077
S1	297.8084	306.0133	0.2083	0.5591	-0.6506	-0.3326
S2	300.5391	313.3448	0.0473	0.4542	-0.4117	-0.1159

Table 9. Minimum and maximum values of LST, NDWI and MNDWI in S0, S1 and S2

Aphid Damage Degree	LST		NDWI		MNDWI	
	Mean value	Standard deviation	Mean value	Standard deviation	Mean value	Standard deviation
S0	290.8578	1.4740	0.3029	0.0574	-0.2293	0.0296
S1	299.9236	1.0834	0.3998	0.0587	-0.4940	0.0362
S2	303.9424	1.7121	0.2979	0.0458	-0.2672	0.0402

Table 10. Mean value and standard derivation of LST, NDWI and MNDWI in S0, S1 and S2

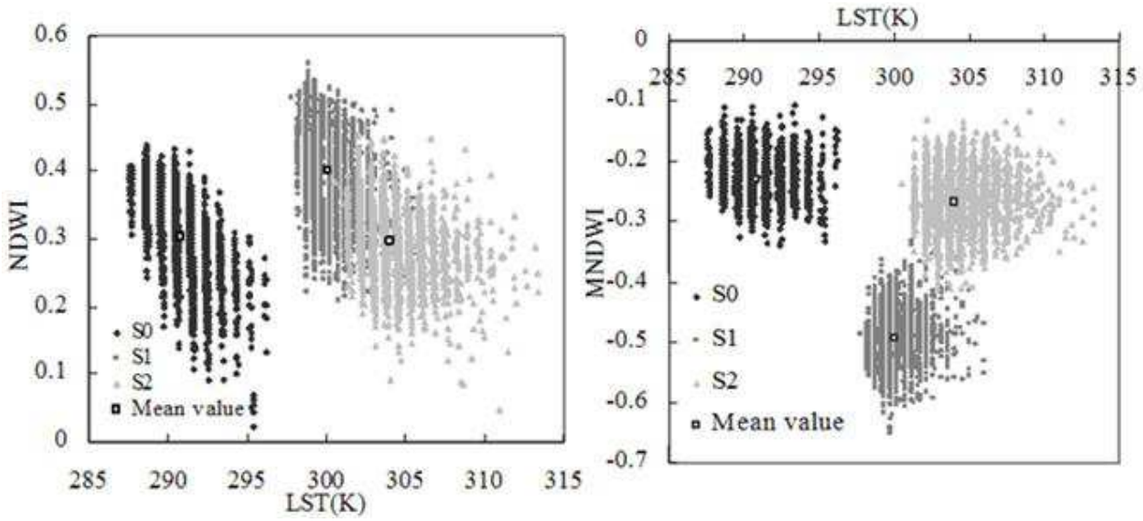

Fig. 21. The distribution of S0, S1 and S2 in the LST-NDWI (left) and LST-MNDWI (right) feature space

3.2.2.2 Discriminating aphid damage degrees using LST and MNDWI

In the 2-dimensional feature space coordinate system that was composed by LST and MNDWI, the S0 samples mainly scattered on the left part of the coordinate system, whereas S1 and S2 samples were distributed on the right part. As shown in Fig. 22, when LST was lower than the certain value, aphid did not occur, suggesting that LST served as a key factor of aphid occurrence and the MNDWI was sensitive to aphid damage degree.

Furthermore, LST_0 and $MNDWI_0$, which were the cutoff value of threshold values of LST and MNDWI of S0, S1 and S2, were determined by mean values and standard deviations. LST0 and MNDWI0 were calculated by formula as follows:

$$LST_0 = LST\_M1 - 2 \times LST\_SD1$$

$$MNDWI_0 = (M\_M1 + 3 \times M\_SD1) + [(M\_M1 + 3 \times M\_SD1) - (M\_M2 - 3 \times M\_SD2)]/2$$

where LST_M1 and LST_SD1 are the mean value and standard deviation of LST for S1; M_M1and M_SD1 are the mean value and standard deviation of MNDWI for S1; and M_M2 and M_SD2 are the mean value and standard deviation of MNDWI for S2.

According to Table 3, LST_0 = 297.7568 and $MNDWI_0$ = -0.3866. Wheat was not infested by aphid when LST< 297.7568, and aphid damage degree was S1 when LST≥297.7568K and -0.6506≤MDNWI ≤-0.3866 and S2 when LST≥297.7568K and -0.3866 ≤MDNWI ≤-0.1077 (Fig. 22).

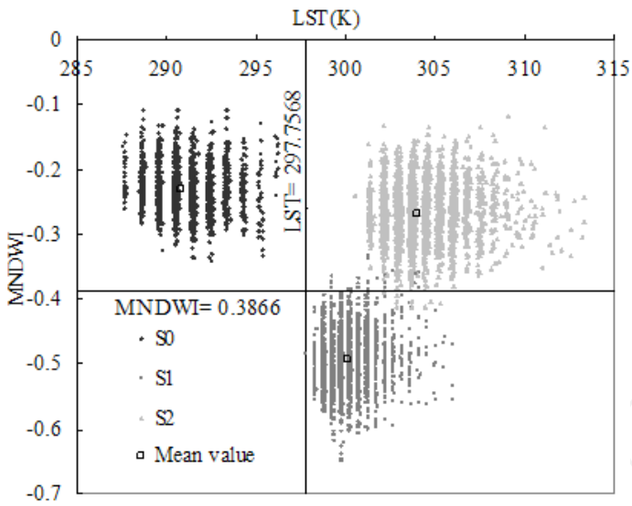

Fig. 22. Discriminating aphid damage degrees using LST and MNDWI

3.2.2.3 Verification

All survey samples, except 20 samples in the subset selection image were used to test the aphid prediction accuracy of 2-dimensional feature space based on LST and MNDWI (Fig. 23).

The discrimination accuracy was assessed using overall accuracy and kappa coefficient (Table 11). The results showed that the overall accuracy was 84%, and the Kappa accuracy was 75.67%.

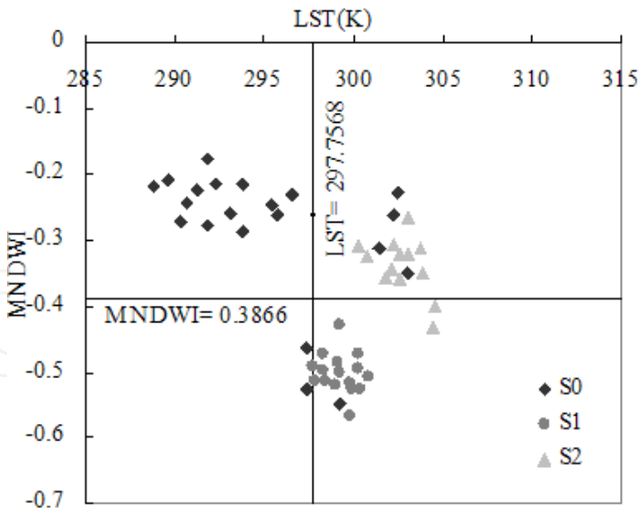

Fig. 23. Distribution of test sample plots in LST-MNDWI feature space

	S0	S1	S2	Total
S0	17	0	0	17
S1	2	14	0	16
S2	4	2	11	19
Total	23	16	11	50

Kappa coefficient = 0.7567

Table 11. Error matrices of the verification samples

3.2.3 Conclusions

This study successfully investigated the relationship between aphid damage degrees and several spectral features, such as NDWI, MNDWI and LST, through 2-dimensional feature space method. The results indicated that LST was the key factor in predicting the occurrence of aphid, and MNDWI was more sensitive to aphid damage degree than NDWI. In the 2-dimension feather space composed by LST and MNDWI, the result showed that S0, S1 and S2 were divided into three regions; S0 was distributed on the left of the space, and S1 and S2 on the right. Further, LST0 and MNDWI0 were calculated according the mean and derivation of S1, S2 as the cutoff value of threshold value to discriminate S0, S1 and S0. Through the verification of discrimination threshold value, it confirmed that the overall accuracy of discrimination was 84% and Kappa coefficient was 0.7567, suggesting that LST and MNDWI were of great potential in discriminating and monitoring the aphid damage degree over a large area, only using thermal infrared band and multi-spectral satellite images.

4. References

Basky Z. & Fónagy A. (2003).Glutenin and gliadin contents of flour derived from wheat infested with different aphid species. *Pest Management Science*, 59, 426-430.

Becker, B. L., David, P. L., & Qi, J. G. (2007). A classification-based assessment of the optimal spectral and spatial resolutions for Great Lakes coastal wetland imagery. *Remote Sensing of Environment*, 108, 111–120

Bravo, C., Moshou, D., West, J., McCartney, A., & Ramon, H. (2003). Early disease detection in wheat fields using spectral reflectance. *Biosystems Engineering*, 84, 137–145.

Broge, N. H., & E. Leblanc. 2000. Comparing prediction power and stability of broadband and hyperspectral vegetation indices for estimation of green leaf area index and canopy chlorophyll density. *Remote Sensing of Environment,* 76, 156–72.

Carlson T. N. & Ripley D. A.. On the relation between NDVI, fractional vegetation cover, and leaf area index. *Remote Sensing of Environment,* 1997, 62(3): 241-252.

Ceccato, P., N. Gobron, S. Flasse, B. Pinty, & S. Tarantola. 2002. Designing a spectral index to estimate vegetation water content from remote sensing data: Part 1. Theoretical approach. *Remote Sensing of Environment*, 82, 188–97.

Christou, P., Twyman, R.M., (2004). The potential of genetically enhanced plants to address food insecurity. *Nutrition Research Reviews* 17, 23–42.

Daughtry, C. S., C. L. Walthall, M. S. Kim, E. Brown de Colstoun, & J. E. McMurtrey.(2000). Estimating corn leaf chlorophyll concentration from leaf and canopy reflectance. *Remote Sensing of Environment*, 74, 229-239.

Fensholt, R., & I. Sandholt.(2003). Derivation of a shortwave infrared water stress index from MODIS near-and shortwave infrared data in a semiarid environment. *Remote Sensing of Environment,* 87, 111–21.

Filella, I., Serrano, L., Serra, J., & Penuelas, J. (1995). Evaluating wheat nitrogen status with canopyreflectance indices and discriminant analysis. *Crop Science*, 35, 1400–1405.

Franke, J., & Menz, G. (2007). Multi-temporal wheat disease detection by multi-spectral remote sensing. *Precision Agriculture*, 8, 161–172.

Galvão, L. S., A. Formaggio, R. & Tisot, D. A. (2005). Discrimination of sugarcane varieties in Southeastern Brazil with EO-1 Hyperion data. *Remote Sensing of Environment*, 94, 523–34.

Gamon, J. A., Penuelas, J., & Field, C. B. (1992). A narrow-waveband spectral index that tracks diurnal changes in photosynthetic efficiency. *Remote Sensing of Environment*, 41(1), 35–44.

Gitelson, A. A., Merzlyak, M. N., & Chivkunova, O. B. (2001). Optical properties and nondestructive estimation of anthocyanin content in plant leaves. *Photochemistry and Photobiology*, 74, 38–45.

Goovaerts, P., Jacquez, G. M., & Marcus, A. (2005). Geostatistical and local cluster analysis of high resolution hyperspectral imagery for detection of anomalies. *Remote Sensing of Environment*, 95, 351–367.

Gong, P., Pu R., Heald R.C.(2002). Analysis of in situ hyperspectral data for nutrient estimation of giant sequoia. *International Journal of Remote Sensing,* 23, 1827-1850.

Haboudane, D., Miller, J. R., Tremblay, N., Zarco-Tejada, P. J., & Dextraze, L. (2002). Integrated narrowband vegetation indices for prediction of crop chlorophyll content for application to precision agriculture. *Remote Sensing of Environment*, 81, 416–426.

Haboudane, D., J. R. Miller, E. Pattery, P. J. Zarco-Tejad, & I. B. Strachan. (2004). Hyperspectral vegetation indices and novel algorithms for predicting green LAI of

crop canopies: Modeling and validation in the context of precision agriculture. *Remote Sensing of Environment,* 90, 337–52.

Hélène L., Frédéric F., Pierre D., Gaétan B., Isztar Z. (2002),Estimation of the spatial pattern of surface relative humidity using ground based radar measurements and its application to disease risk assessment. *Agricultural and Forest Meteorology*, 111, 223-231.

Huang, W. J., David, W. L., Niu, Z., Zhang, Y. J., Liu, L. Y., & Wang, J. H. (2007). Identification of yellow rust in wheat using in situ spectral reflectance measurements and airborne hyperspectral imaging. *Precision Agriculture*, 8, 187–197.

Hunt E.R., Rock B.N. (1989). Detection of changes in leaf water content using Near- and Middle-Infrared reflectances. *Remote Sensing of Environment*, 30, 43-54.

Jiménez-Muñoz J. C., Sobrino J. A. & Leonardo P. (2004). Land Surface Temperature Retrieval from Landsat TM 5. *Remote Sensing of Environment*, 90, 434-440.

Kaufman Y. J. & Gao B. C. (1992). Remote Sensing of Water Vapor in the Near IR from EOS/MODIS. *IEEE Transactions on Geoscience and Remote Sensing*, 30, 871-884.

Kim, M. S., C. S. T. Daughtry, E. W. Chappelle, & J. E. McMurtrey. 1994. The use of high spectral resolution bands for estimating absorbed photosynthetically active radiation (APAR). *In Proceedings of the 6th International Symposium on Physical Measurements and Signatures in Remote Sensing*, 299–306.

Li, G. B., Zeng, S. M., & Li, Z. Q. (1989). Integrated Management of Wheat Pests (pp. 185–186). Beijing: Press of Agriculture Science and Technology of China (in Chinese).

Luo, J. H., Zhang, J. C., Huang, W. J., Xu, X. G., Jin, N. (2010). Preliminary study on the relationship between land surface temperature and occurrence of yellow rust in winter wheat. *Disaster Advances,* 3, 288-292.

Luo, J. H., Huang, W. J., Zhang, J. C., Xu X. G. & Wang D. C. (2011). The preliminary study on spectral response of wheat under different stresses between field and satellite remote sensing. *Sensor Letters,* 9, 1225-1228.

Merton, R., & J. Huntington.(1999). Early simulation of the ARIES-1 satellite sensor for multi-temporal vegetation research derived from AVIRIS. In *Summaries of the Eight JPL Airborne Earth Science Workshop*, 9–11 February, 299–307. Pasadena, CA: JPL Publication 99-17.

Moshou, D., Bravo, C., West, J., Wahlen, S., McCartney, A., & Ramon, H. (2004). Automatic detection of 'yellow rust' in wheat using reflectance measurements and neural networks. *Computers and Electronics in Agricultur*e, 44, 173–188.

Peñuelas, J., Baret, F., & Filella, I.(1995). Semi-empirical indices to assess carotenoids/chlorophyll a ratio from leaf spectral reflectance. *Photosynthetica*, 31, 221–230.

Merzlyak, M. N., Gitelson, A. A., Chivkunova, O. B., & Rakitin, V. Y. (1999). Non-destructive optical detection of pigment changes during leaf senescence and fruit ripening. *Physiologia Plantarum*, 106, 135–141.

Peñuelas, J., Gamon, J. A., Fredeen, A. L., Merino, J., & Field, C. B. (1994). Reflectance indices associated with physiological changes in nitrogen- and water-limited sunflower leaves. *Remote Sensing of Environment*, 48, 135–146.

Peñuelas, J., J. Piñol, R. Ogaya, & I. Filella. (1997). Estimation of plant water concentration by the reflectance water index WI (R900/R970). *International Journal of Remote Sensing,* 18, 2869–75.

Pu, R., Ge S., Kelly N.M., Gong P. (2003). Spectral absorption features as indicators of water status in coast live oak (Quercus agrifolia) leaves. *International Journal of Remote Sensing*, 24, 1799-1810.

Pu, R., Foschi L., Gong P. (2004). Spectral feature analysis for assessment of water status and health level in coast live oak (Quercus agrifolia) leaves. *International Journal of Remote Sensing*, 25, 4267-4286.

Rouse, J. W., R. H. Haas, J. A. Schell, & D. W. Deering.(1973). Monitoring vegetation systems in the Great Plains with ERTS. *Proc 3rd ERTS Symp* 1, 48–62.

Rosenfield G. & Fitzpatrick-Lins K. (1986). A coefficient of agreement as a measure of thematic classification accuracy. *Photogrammetric Engineering and Remote Sensing,* 52, 223-227.

Rules for Resistance Evaluation of Wheat to Diseases and Insect Pests Part 7: Rule for Resistance Evaluation of Wheat to Aphids. NY/T 1443.7-2007

Raikes, C., & L. L. Burpee. (1998). Use of multispectral radiometry for assessment of Rhizoctonia blight in creeping bentgrass. *Phytopathology*, 88, 446-449.

South, S., Qi, J. G., & Lusch, D. P. (2004). Optimal classification methods for mapping agricultural tillage practices. *Remote Sensing of Environment*, 91, 90–97

Susan E. Halbert, June Connelly B., Bishop G. W., et al. (1992).Transmission of barley yellow dwarf virus by field collected aphids (Homoptera: Aphididae) and their relative importance in barley yellow dwarf epidemiology in southwestern Idaho. *Annals of Applied Biology*, 121, 105-121.

Strange, R.N., Scott, P.R., (2005). Plant Disease: A Threat to Global Food Security. *Annual review of Phytopathology*, 40, 83–116.

Sutton, J.C., Gillespie, T.J., Hildebrand, P.D. (1984). Monitoring weather factors in relation to plant disease. *Plant Disease*, 68, 78–84.

Thenkabail, P. S., Smith, R. B., & De Pauw, E. (2000). Hyperspectral vegetation indices and their relationships with agricultural crop characteristics. *Remote Sensing of Environment*, 71, 158–182.

West, J. S., Bravo, C., Oberti, R., Lemaire, D., Moshou, D., & McCartney, H. A. (2003). The potential of optical canopy measurement for targeted control of field crop disease. *Annual Reviews of Phytopathology*, 41, 593–614.

Xiao, Z. Q., Li, Z. M., Fan M., Zhang, Y. Ma, S. j. (2007), Prediction model on stripe rust influence extent of winter wheat in Longnan Mountain area. *Chinese Journal of Agrometeorology*, 28, 350-353.

Yu, B., Ostland, I.M., Gong, P., Pu, R. L. (1999) Penalized discriminant analysis of in situ hyperspectral data for conifer species recognition. *IEEE Transactions on geosciences and remote sensing*, 37, 2569-2577.

Zarco-Tejada, P. J., A. Berjón, R. López-Lozano, J. R. Miller, P. Martín, V. Cachorro, M. R. González, & A. Frutos. (2005). Assessing vineyard condition with hyperspectral indices: Leaf and canopy reflectance simulation in a row-structured discontinuous canopy. *Remote Sensing Environment*, 99:271–87.

Zeng, S. M. (2003). Simulation study on oversummering process of wheat stripe rust caused Puccinia striiformis west. *In China, Acta Phytopathologica Sinica*, 33, 267-278.

Zhang, M. H., Qin, Z. H., Liu, X., & Ustin, S. L. (2003). Detection of stress in tomatoes induced by late blight disease in California, USA, using hyperspectral remote sensing. *International Journal of Applied Earth observation and Geo information*, 4, 295–310.

Zhang, J. C., Huang, W. J., Li, J. Y., Yang, G. J., Luo, J. H., Gu, X. H., & Wang, J. H. (2011). Development, evaluation and application of a spectral knowledge base to detect yellow rust in winter wheat. *Precision Agriculture,* 12, 716-731.

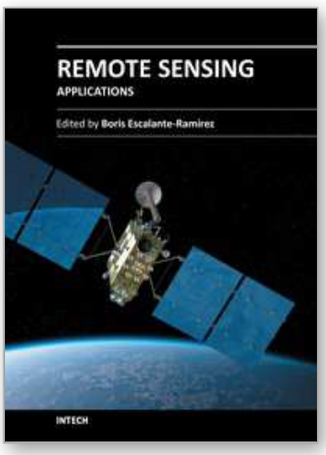

Remote Sensing - Applications
Edited by Dr. Boris Escalante

ISBN 978-953-51-0651-7
Hard cover, 516 pages
Publisher InTech
Published online 13, June, 2012
Published in print edition June, 2012

Nowadays it is hard to find areas of human activity and development that have not profited from or contributed to remote sensing. Natural, physical and social activities find in remote sensing a common ground for interaction and development. This book intends to show the reader how remote sensing impacts other areas of science, technology, and human activity, by displaying a selected number of high quality contributions dealing with different remote sensing applications.

How to reference
In order to correctly reference this scholarly work, feel free to copy and paste the following:

Wenjiang Huang, Juhua Luo, Jingcheng Zhang, Jinling Zhao, Chunjiang Zhao, Jihua Wang, Guijun Yang, Muyi Huang, Linsheng Huang and Shizhou Du (2012). Crop Disease and Pest Monitoring by Remote Sensing, Remote Sensing - Applications, Dr. Boris Escalante (Ed.), ISBN: 978-953-51-0651-7, InTech, Available from: http://www.intechopen.com/books/remote-sensing-applications/crop-disease-and-pest-monitoring-by-remote-sensing

INTECH
open science | open minds

InTech Europe
University Campus STeP Ri
Slavka Krautzeka 83/A
51000 Rijeka, Croatia
Phone: +385 (51) 770 447
Fax: +385 (51) 686 166
www.intechopen.com

InTech China
Unit 405, Office Block, Hotel Equatorial Shanghai
No.65, Yan An Road (West), Shanghai, 200040, China
中国上海市延安西路65号上海国际贵都大饭店办公楼405单元
Phone: +86-21-62489820
Fax: +86-21-62489821

IntechOpen